Microphysical controls on the isotopic composition of wintertime orographic precipitation

M. Moore,[1] P. N. Blossey,[2] A. Muhlbauer,[2,3,4] and Z. Kuang[1,5]

Key Points

- Distinct isotopic signatures of microphysical processes can be determined.
- Temperature and mountain height control precipitation isotopic composition more strongly than CDNC.
- Microphysical changes with CDNC, temperature, and mountain height establish isotopic composition.

Mary Moore, Department of Earth and Planetary Sciences, Harvard University, Cambridge, MA 02138, USA. (moore3@fas.harvard.edu)

[1]Department of Earth and Planetary

Abstract. The sensitivity of mixed-phase orographic clouds, precipitation and their isotopic content to changes in dynamics, thermodynamics and microphysics is explored in idealized two-dimensional flow over a mountain barrier. These simulations use the Weather Research and Forecasting (WRF) Model with stable water isotopologues (HDO and $H_2^{18}O$), which have been integrated into the Thompson microphysics scheme within WRF as part of the present project. In order to understand how the isotopic composition of

Sciences, Harvard University, Cambridge, MA, USA.

[2]Department of Atmospheric Sciences, University of Washington, Seattle, WA, USA.

[3]Joint Institute for the Study of the Atmosphere and Ocean, Department of Atmospheric Sciences, University of Washington, Seattle, WA, USA

[4]FM Global Research,Norwood, MA, USA.

[5]School of Engineering and Applied Sciences, Harvard University, Cambridge, MA, USA.

precipitation ($\delta^{18}O_{precip}$) is fixed, the mountain height, temperature, and the prescribed cloud droplet number concentration (CDNC) have been varied in a series of simulations. For the given range of values explored in this work, changes in mountain height and temperature induce stronger responses in domain-averaged $\delta^{18}O_{precip}$ than do changes in CDNC by a factor of approximately 10. The strongest response to changing CDNC leads to local variations of $\delta^{18}O_{precip}$ of about 3‰, though those occur in regions of weak precipitation (<0.1 mm hr^{-1}). Changes in $\delta^{18}O_{precip}$ can be understood through the microphysical pathways by which precipitable hydrometeors are formed and by the isotopic signature associated with each pathway. The decrease in $\delta^{18}O_{precip}$ with increasing mountain height is not just a function of decreasing temperature, but also reflects the changing contributions and distinct isotopic signatures of riming of cloud liquid and vapor deposition onto snow, the leading sources of precipitation in these simulations. The changes in $\delta^{18}O_{precip}$ with mountain height, temperature and CDNC are governed in part by the microphysical pathways through which precipitating hydrometeors are formed and grow.

1. Introduction

Precipitation that forms due to interaction with mountain barriers, or orographic precipitation, is an important contributor to surface water resources. In particular, runoff from rainfall and melting of the mountain snowpack feed into river basins that provide water to a number of heavily populated regions. As the amount and location of precipitation on the mountain barrier will determine the volume of runoff and the watershed into which it flows, understanding all of the factors that influence and control orographic precipitation is essential for current and future forecasts of this necessary resource.

There have been extensive regional studies regarding the formation and behavior of orographic precipitation [e.g. *Hobbs*, 1975; *Smith et al.*, 2005; *Smith and Evans*, 2007; *Zubler et al.*, 2011]. The total precipitation and its spatial distribution have been found to be dependent upon several variables, including the orientation and geometry of the terrain, atmospheric stability, orographic flow dynamics and cloud microphysics [e.g. *Colle*, 2004; *Galewsky*, 2008; *Muhlbauer and Lohmann*, 2008]. In terms of cloud microphysics, the different pathways through which precipitating hydrometeors grow can be more or less efficient and thus greatly influence the amount of precipitation. For example, in mixed-phase orographic clouds, the growth and fallout of snow and graupel may be enhanced by the "seeder-feeder" mechanism [*Reinking et al.*, 2000], wherein ice crystals grow by vapor deposition in an ice cloud aloft before sedimenting to lower levels in the cloud where the ice continues to grow by collecting cloud droplets (riming). This enhanced low-level riming increases the fallspeed of snow and also the overall precipitation efficiency of the cloud [*Mitchell et al.*, 1990; *Borys et al.*, 2003], thereby augmenting precipitation on the

windward side of the mountain at the expense of the transport of hydrometeors to the leeward slope (and the resulting precipitation there, which is known as "spillover").

The stable isotopologues of water ($H_2^{16}O$, HDO, $H_2^{18}O$) have been used in precipitation analysis dating back to the initial work of *Dansgaard* [1952]. In the mid-latitudes, where westerlies impinging on north-south oriented mountain ranges form the motivation for our idealized simulations, the isotopic composition of precipitation is primarily temperature-dependent [e.g. *Dansgaard*, 1964; *Noone and Simmonds*, 2002; *Jouzel*, 2003; *Lee et al.*, 2007], such that the ratio of the heavy (e.g., $H_2^{18}O$) to light ($H_2^{16}O$) isotopes correlates positively with temperature. In mountainous regions, the relationship between the isotopic composition of precipitation and temperature is additionally linked with altitude [*Dansgaard*, 1964]. Air cools as it rises along the upslope on the windward side of a mountain, and the progressive removal of precipitation produces a gradient in the isotopic composition with altitude. This leads to precipitation enriched in heavy isotopes forming at lower altitudes, and more depleted precipitation (i.e., with lower isotopic ratios) at higher altitudes, as well as on the downslope in the lee of the mountain peak [*Smith et al.*, 2005]. This isotopic gradient was connected to the fractional removal of water by a mountain barrier and its drying ratio by *Smith et al.* [2005]. The relationship between isotopic composition and altitude has also been used to relate paleoclimate proxies for the isotopic composition of precipitation to past mountain elevation [*Poage and Chamberlain*, 2001; *Rowley et al.*, 2001]. However, as demonstrated by *Galewsky* [2009] and *Lechler and Galewsky* [2013], in different dynamical regimes, the airflow over the mountain can complicate the relationship between the isotopic composition of precipitation and the altitude of a mountain barrier.

In addition to the dynamical influences on orographic precipitation and its isotopic content, microphysical processes can also modify the isotopic signature of precipitation. *Coplen et al.* [2015] connected variations in the isotopic content of precipitation in land-falling extratropical cyclones with changes in the storm structure and different pathways of precipitation formation. Observations of snowfall from the Sierra Nevada [*Demoz et al.*, 1991] and snowfall and cloud liquid in Colorado [*Lowenthal et al.*, 2011] suggested that the isotopic composition of snowfall is influenced by the degree of riming. By sampling both the isotopic and chemical composition of both snowfall and cloud droplets at a mountain-top site in Colorado, *Lowenthal et al.* [2011] related the degree of riming of snowfall to the chemical composition of the snow and concurrently sampled cloud droplets. They found that snow mass formed mainly through riming was more enriched and had an isotopic signature that was similar to the cloud droplets. This relationship was then employed to make predictions about the altitude at which snow formed through vapor deposition.

The relative role of riming in mixed-phase orographic precipitation can be reduced by decreasing temperature, through the glaciation of liquid clouds, and by increasing aerosol concentrations, which tend to lead to more numerous and smaller cloud droplets that are less likely to be collected by falling snow [*Pruppacher and Klett*, 1997; *Wang and Ji*, 2000]. Increased aerosol concentrations can also suppress or delay the formation of precipitation in liquid-only clouds by reducing the efficiency of collision and coalescence processes [*Albrecht*, 1989; *Ramanathan et al.*, 2001]. While aerosols have the potential to impact individual microphysical processes that contribute to precipitation, their influence on the amount and distribution of orographic precipitation has not been definitely established and appears to depend strongly on the environmental conditions of the region

being considered [*Borys et al.*, 2000, 2003; *Khain and Pokrovsky*, 2004; *Lynn et al.*, 2007; *Muhlbauer and Lohmann*, 2008; *Saleeby et al.*, 2013]. In a study of warm (liquid-only) orographic clouds and precipitation, *Miltenberger et al.* [2015] suggested that interactions between dynamical and microphysical processes can lead to regimes where the precipitation and the precipitation efficiency are insensitive to changes in cloud droplet number concentration (CDNC), which is used as a proxy for aerosol concentrations.

To explore how such changes in microphysical processes influence mixed-phase orographic precipitation and its isotopic content, we perform a number of idealized two-dimensional simulations in which the mountain height, temperature and CDNC are varied. Particular attention is paid to changes in the microphysical processes that contribute to the growth of precipitating hydrometeors and how those processes and their isotopic signatures control the amount, distribution and isotopic content of precipitation in these experiments. By tracking the isotopic ratio associated with precipitation growth processes within these simulations, we determine if each microphysical process has a distinct isotopic signature and how each process contributes to the overall isotopic signal of precipitation in different regimes.

Although the results presented in this paper are based on idealized simulations, they represent a step towards constructing an isotope-enabled regional modeling capability for WRF. Previous work with isotope-enabled global models [e.g. *Noone and Simmonds*, 2002; *Vuille et al.*, 2003; *Lee et al.*, 2007; *Field*, 2010] has advanced our knowledge of how large-scale processes affect isotopic composition. However, the limitations of global climate models (GCMs) in representing topography and cloud-scale processes leaves room for higher-resolution regional models that more faithfully represent such fine-scale phenomena

[*Prein et al.*, 2015]. The work of *Pfahl et al.* [2012] provides an example of how a fine-scale regional model can improve the representation of isotopic signals over that of an isotope-enabled GCM. By using a regional model with horizontal grid spacing of $O(1$ km), this work aims to understand orographic precipitation resolving scales much finer than those represented in a typical isotope-enabled GCM whose horizontal grid spacings vary from approximately 200 to 400 km [*Conroy et al.*, 2013].

2. Model and Experiments

2.1. Model Setup

To conduct the orographic precipitation experiments, we use the WRF model version 3.5.1 [*Skamarock and Klemp*, 2008] provided by the Mesoscale and Microscale Meteorology Division of the National Center for Atmospheric Research. The model is configured to perform simulations of idealized 2D flow over a hill. The domain consists of 300 grid points with 2 km spacing in the horizontal direction and 105 vertical levels whose spacing varies from 25-200 m in the lower 5 km and is uniform above 5 km. The duration of each simulation is twelve hours. The Thompson microphysics scheme [*Thompson et al.*, 2008] was chosen for this work because a study of wintertime precipitation in a mountainous region of the western United States found that, along with one other scheme, the Thompson microphysics scheme provided the best representation of cold season snowfall [*Liu et al.*, 2011]. In addition, the Thompson scheme includes a detailed treatment of the riming of cloud droplets by snow (as in *Saleeby and Cotton* [2008]), which has proved important for realistic simulation of the effects of pollution on riming in mixed-phase orographic clouds [*Lohmann*, 2004; *Saleeby and Cotton*, 2008; *Saleeby et al.*, 2011].

As noted previously, different atmospheric regimes are simulated in order to study the response of model microphysics. The Thompson microphysics scheme allows the user to specify the CDNC value, which is utilized in this work as a proxy for aerosols. The chosen CDNC values represent conditions that range from pristine to polluted. The working assumption is that for high aerosol loading, there are more cloud condensation nuclei (CCN) and thus a higher CDNC value, while a lower CDNC value indicates a scenario with few aerosols and therefore fewer CCN. More specifics about the experimental setup are given in section 2.3.

2.2. Isotopic implementation

In its default configuration, the Thompson scheme only treats microphysical transfers of the standard isotopologue of water ($H_2^{16}O$) among water vapor and the different hydrometeors included in the scheme: cloud liquid, rain, cloud ice, snow and graupel. As part of the present project, we have extended the Thompson scheme so that the microphysical transfers of the stable isotopologues of water (HDO and $H_2^{18}O$) are also included. The isotopic composition of water vapor and each hydrometeor is tracked, and the exchanges of the heavy isotopologues of water are accounted for during each microphysical process represented in the Thompson scheme. Isotopic fractionation — the unequal exchange of heavy and lighter isotopologues of water — is accounted for in processes that involve the deposition of vapor onto liquid or ice hydrometeors and those involving the evaporation of liquid phase hydrometeors (rain or cloud liquid). Other processes that involve the transfer of whole hydrometeors from one category to another (e.g., freezing, melting, riming), occur without fractionation. As in *Bony et al.* [2008], *Blossey et al.* [2010] and *Pfahl et al.* [2012], the sublimation of ice phase hydrometeors (snow, cloud ice, graupel) is also

assumed to occur without fractionation, so that the vapor produced by sublimation of snow, for example, has the same isotopic composition as the snow. While sublimation is expected to produce vapor from the outer shell of an ice phase hydrometeor, and this layer may not have the same isotopic composition as the particle as a whole, tracking the composition of individual layers within the crystals is judged to be too complicated and expensive to include in the present implementation. Note that the implementation, which follows *Blossey et al.* [2010], includes few approximations in its representation of isotopic exchanges beyond the assumption that the isotopic composition of each hydrometeor category in a given grid cell is uniform and that no fractionation occurs during sublimation. The model uses time steps on the order of a few seconds, so that only cloud liquid and vapor are assumed to equilibrate within a single time step. Other processes are integrated in time explicitly by the model. A more detailed description of the water isotope physics is given in Appendix A.

The quality of the isotopic simulation depends strongly on the representation of the standard isotopologue of water. If the microphysics scheme and the broader model do a poor job in representing the amount and distribution of precipitation of the standard isotopologue of water, this will be reflected in the isotopic composition as well. Encouraged by the performance of the Thompson scheme within WRF on wintertime orographic precipitation [*Liu et al.*, 2011] and by the representation of isotopic composition in tropical convection in a similar implementation of water isotopologues in *Blossey et al.* [2010], we proceed with the simulations here.

For the isotopic analysis, our results on $H_2^{18}O$ are presented in delta-notation such that $\delta^{18}O = 1000\left(\frac{R}{R_o} - 1\right)$, where R is the isotopic ratio of $H_2^{18}O$ in a specified water

187 species and R_o is the isotopic ratio of the standard. While HDO is also included in the
188 microphysics scheme, the additional information that can be gained by considering both
189 HDO and $H_2^{18}O$ will be left to future work.

2.3. Experimental Setup

190 Several experiments are conducted that alter the initial temperature profile, mountain
191 height (800, 1500 and 3000 m), and the CDNC (25, 100, 200, 400, and 800 cm^{-3}). Two
192 initial temperature profiles are used here and are referenced as warm or cold based on the
193 surface temperature of the upstream sounding (T_{sfc} = 7°C and 0°C, respectively). Ex-
194 periments are referenced by abbreviations (e.g., W800m), which indicate the temperature
195 sounding (W=warm or C=cold) and mountain height settings. The setup and initial con-
196 ditions, including the temperature profiles, are similar to those in *Muhlbauer et al.* [2010],
197 with a mountain half-width of 20 km and a horizontal wind profile that is a constant
198 15 m s^{-1} below 10 km and linearly increases to 40 m s^{-1} at the top model layer (30 km).
199 To generate the initial vapor conditions for $H_2^{18}O$ and HDO, a Rayleigh distillation
200 profile is generated assuming equilibrium with ocean water at 20°C, which represents the
201 average temperature of the ocean surface where the initial isotopic signature of the air
202 mass will be set. The model's initial conditions for the isotopic content of water vapor are
203 interpolated from this Rayleigh profile based on the water vapor mass mixing ratio. As
204 the cold sounding is drier than the warm sounding, it is also more depleted, such that the
205 $\delta^{18}O$ of vapor at the surface is 8‰ less than that of the warm sounding. Neither liquid
206 nor ice condensate exists initially, and therefore their isotopic compositions do not need
207 to be initialized.

2.4. Model Validation

The model's ability to simulate orographic clouds and precipitation is on par with previous studies. The results are very similar to the WRF simulations in *Muhlbauer et al.* [2010], despite the use of a different microphysical scheme. There are some small differences in the simulated orographic clouds, and our experiments produce more accumulated precipitation. However, these deviations can be attributed to our implementation of a longer simulation time and a larger range of CDNC values in addition to the choice of microphysical scheme. The changes in the liquid orographic cloud are also similar to results seen by *Xiao et al.* [2014], who also used the same idealized WRF setup, but coupled with a detailed bin microphysics scheme and a warmer initial temperature profile. The evolution of cloud liquid and microphysical processes as CDNC increases in our cold experiments is similar to that of *Saleeby et al.* [2006], who used the Colorado State University - Regional Atmospheric Modeling System with a different microphysics scheme to simulate realistic wintertime orographic clouds in northern Colorado.

This project represents the first use of this isotope-enabled version of the Thompson scheme within WRF. As the present modeling study is idealized and the incorporation of water isotopologues into the real-case forecasting capability of WRF is not complete, we focus on the performance of the scheme within the present simulations. First, the isotopic composition of precipitation along the upslope of the mountain approximately conforms to that of a Rayleigh process and is slightly more depleted than the Rayleigh process due to dynamical effects of the mountain [*Galewsky*, 2009] and the formation of precipitation from more depleted vapor above the surface of the mountain (supplemental Fig. S1). Second, in section 3.3, closed budgets for the surface precipitation are constructed that explain

the precipitation itself and its isotopic composition in terms of the various microphysical processes that contribute to the formation and growth of precipitating hydrometeors. Last, the isotopic composition of water vapor and hydrometeors described in sections 3.1 and 3.4 shows the expected influence of microphysical processes on isotopic composition, such as isotopic equilibration of cloud liquid and water vapor, vapor deposition onto ice and the evaporation of rain in subsaturated conditions.

It should also be noted that the average δ^{18}O values of total precipitation compare well with observations in conditions similar to those used here for initial conditions. *Anderson et al.* [2015] calculated the average δ^{18}O of snowpack using the Isotopes in Rocky Mountain Snowpack (IRMS) database, and found that values ranged between -10‰ and -25‰, which compares well with the range of δ^{18}O in the average precipitation for our experiments (approximately -10‰ to -16‰ in warm simulations and -19‰ to -26‰ in cold experiments). Comparable $\delta^{18}O_{precip}$ values (-12‰ to -24‰) were measured during a 1985 March storm in Kingvale, CA, which is located upwind of the Sierra Nevada crest at an elevation of 1859 m [*Warburton et al.*, 1993]. *Warburton and DeFelice* [1986] analyzed samples in the Central Sierra Nevada, and found that snow formed through vapor deposition had a δ^{18}O signature that ranged from -18.4‰ to -22.9‰, which corresponds well with our cold temperature profile experiments (see further discussion in section 3). The snow samples from the same study that indicated growth by a combination of riming and vapor deposition, were less depleted and ranged between -6.4‰ and -16.8‰, which resembles results in our warm simulations (see section 3). Values similar to *Warburton and DeFelice* [1986] were measured in Colorado by *Lowenthal et al.* [2011] for snow that had undergone little riming. In the same study, snow that experienced more riming (as in-

dicated by higher concentrations of sulfate), was less depleted and ranged between -15.6‰ and -20.4‰.

3. Model Results

3.1. Reference Simulation

To outline the general characteristics of the cloud and precipitation in these simulations, the simulation with the warmer sounding ($T_{sfc} = 7°$C), a 800 m high mountain, and a cloud droplet number concentration (CDNC) of 200 cm^{-3} is chosen as the reference simulation. Fig. 1b shows the average simulated mass of cloud liquid along with the combined mass of cloud ice and snow for the reference simulation. (Figs. 1a and 1c will be discussed in section 3.2.) The figure combines cloud ice and snow together, as the setup of the Thompson scheme quickly leads to the conversion of cloud ice to snow, and as a result, produces little cloud ice [*Thompson et al.*, 2008]. Note that while a wave cloud exists aloft and downstream of the mountain in these simulations, our focus is on the cloud and precipitation over the mountain, where almost all precipitation is produced.

The orographic cloud in the reference simulation does not extend higher than 4 km and has a much higher mass of cloud liquid than a combined mass of snow and ice (Fig. 1b). The frozen hydrometeors occur predominately upstream of the mountain peak with only a little spillover ($\sim$10 km) to the downstream side. For the most part, the liquid and ice/snow regions of the cloud overlap, except on the leeward slope, where the glaciated cloud is located above the liquid one.

The isotopic values of vapor, cloud liquid, rain and ice/snow for the reference simulation are presented in Fig. 2. Cloud liquid isotopic values range from approximately -7‰ near the mountain surface to -22‰ at cloud top (Fig. 2c). Isotopic equilibrium is

enforced between cloud liquid and vapor, so that decreasing δ^{18}O of cloud liquid with height is expected given that the vapor δ^{18}O shows the same trend (Figs. 2a and 2c). The cloud liquid that extends further leeward has roughly the same δ^{18}O value as the cloud liquid on the corresponding windward side, so there is no obvious δ^{18}O difference between the windward and leeward cloud liquid. As expected from rainout (i.e., the progressive removal of heavy isotopologues by precipitation across the mountain barrier [*Clark and Fritz*, 1997; *Smith et al.*, 2005]), the δ^{18}O of water vapor does show asymmetry about the mountain and is more depleted at low levels further downstream of the mountain. The cloud ice/snow δ^{18}O values range from -10‰ near cloud base to -35‰ at cloud top (Fig. 2d).

Fig. 3a shows the profile of accumulated precipitation across the mountain for the reference simulation along with a number of different CDNC concentrations. (The sensitivity to CDNC will be discussed in the following section.) The precipitation for the reference simulation (CDNC = 200 cm^{-3}, red line) peaks over the mountain top and is nearly symmetric, with slightly more precipitation falling downwind of the peak and a spillover ratio of 0.56 (Tab. 1). (The spillover ratio is the ratio of the accumulated leeward precipitation to total precipitation.) Most of the precipitation falls as rain at the surface, with similar, smaller amounts of snow and graupel (Tab. 1). The isotopic composition of the accumulated precipitation $\delta^{18}O_{precip}$ in the reference simulation (Fig. 3b, red line) becomes more enriched as one ascends the lower slope on the upwind side of the mountain. This is also seen in the isotopic composition of rain in Fig. 2b, and is associated with a shift from rain resulting from the melting of snow that was formed aloft through vapor deposition, to rain and snow that grew through the conversion and accretion of cloud liquid. Such changes

in the microphysical pathways through which precipitating hydrometeors are formed and their impact on $\delta^{18}O_{precip}$ will be discussed in greater detail in section 3.3. Following this peak in $\delta^{18}O_{precip}$ at x=280 km, the isotopic composition of precipitation falls off across the mountain as the heavier isotopes are removed preferentially through fallout. As noted in the introduction, this may be modeled approximately as a Rayleigh process [*Smith et al.*, 2005], though there are some complications due to dynamical response to topography [*Galewsky*, 2009] and microphysical effects. The increase in $\delta^{18}O_{precip}$ on the downslope at x=315-320 km is associated with the fractionation of evaporating rain once it passes downstream of the orographic cloud (see also Fig. 2b-c.) As shown in previous studies [e.g. *Stewart*, 1975; *Lawrence et al.*, 1998; *Bony et al.*, 2008; *Risi et al.*, 2008], evaporation in subsaturated conditions tends to enrich the rain and deplete the vapor, as the lighter H_2O will more quickly move from the liquid to the surrounding vapor.

3.2. Sensitivity to CDNC

Next, the sensitivity of the reference simulation to changes in CDNC (as a proxy for aerosol variations) is shown. This is interesting both as a way to understand whether aerosol impacts on orographic precipitation [e.g., *Rosenfeld et al.*, 2008] could impact the isotopic composition as well, and as an example of how changing the microphysical processes which contribute to precipitation could impact the amount, distribution and isotopic composition of orographic precipitation.

Three cases with increasing values of CDNC are shown in Fig. 1, which illustrates potential changes in the orographic cloud with CDNC. As the CDNC value increases, the conversion of cloud to rain and the riming of cloud liquid by snow become less efficient, resulting in an increase in both the amount of cloud liquid and the leeward region it spans.

While there is already leeward spillover of cloud liquid in the 25 cm^{-3} case, cloud liquid extends an additional 15 km down the leeward side in the 800 cm^{-3} experiment, with the region of maximum mass mixing ratio (red filled contours) also reaching approximately 5 km further downstream. This shift in the leeward extent of cloud liquid is mirrored in the isotopic composition of precipitation in Fig. 3b, where the increase in $\delta^{18}O_{precip}$ due to rain evaporation occurs farther downstream as CDNC increases. On the windward slope, the location of the leading edge of the cloud does not change in all of the warm 800 m experiments. Increases in CDNC have little impact on the location of snow and cloud ice: both the horizontal and vertical extent of the glaciated cloud remain the same. The mass mixing ratio, however, does decrease very slightly (note change in contours over the mountain peak region) as the CDNC increases, which is opposite to and of much smaller magnitude than the trend found for cloud liquid. The isotopic signatures of cloud liquid and combined cloud ice/snow are similar to those of the reference simulation (Fig. 2) and are not shown.

As in the reference simulation, most of the precipitation in the simulations with varying CDNC falls as rain (see Tab. 1) with small, similar amounts of accumulated snow and graupel. The third column in Tab. 1 indicates that the accumulated precipitation decreases as CDNC increases, and is reduced by more than half between the 25 cm^{-3} and 800 cm^{-3} experiments. Fig. 3a shows that the location of the maximum precipitation shifts leeward as CDNC increases, which has been previously observed in wintertime orographic precipitation [*Jirak and Cotton*, 2006; *Saleeby et al.*, 2011]. Among the different mountain heights and temperatures considered here, the magnitude of the shift is strongest and most obvious for the W800m experiments, where there is a difference

of approximately 10 km between the precipitation peaks in the 25 cm^{-3} and 800 cm^{-3} simulations. This shift is also evident in the spillover calculations in Tab. 1.

The domain can be broken down into three smaller regions: upstream of the peak (up to 290 km into the domain), around the peak (290–310 km) and downstream of the peak (310 km onwards). As Fig. 3a indicates, most of the precipitation falls in the first and second regions. The influence of CDNC on precipitation is also most pronounced in these regions. However, the CDNC impact on the $\delta^{18}O_{precip}$ is slightly different. Fig. 3b illustrates that the largest $\delta^{18}O_{precip}$ difference between simulations occurs in the first region, but over the second region, variation in the isotopic signal is small ($\leq 1‰$). In the third region, downstream of the mountain peak, the accumulated precipitation is relatively unchanged between simulations, but there is some separation in the $\delta^{18}O_{precip}$ of approximately 2‰ at x=310 km before the effects of rain evaporation enter further down the lee slope. The slopes of $\delta^{18}O_{precip}$ across the peak differ, with the steepest change in $\delta^{18}O_{precip}$ across the peak in the simulation with the largest precipitation (CDNC=25 cm^{-3}) as one would expect due to the effect of rainout [*Smith et al.*, 2005]. This leads the 25 cm^{-3} simulation to have the largest upstream-downstream difference in $\delta^{18}O_{precip}$ around the peak (x=290–310 km).

3.3. Microphysical pathways

To better understand the changes in precipitation and its isotopic composition across the mountain, we consider the budget for the total mass of precipitating hydrometeors (rain, snow and graupel combined) in these simulations, integrated in time and over the whole domain or a sub-region of the domain. Since isotopic composition is unchanged by exchanges between rain, snow and graupel by freezing, melting or aggregation, we focus

on the sources which determine the isotopic composition of the precipitation: autoconversion/accretion of cloud liquid or cloud ice, riming of cloud liquid and exchanges with vapor by deposition or sublimation/evaporation. In this budget, surface precipitation, P, is a sink of hydrometeor mass and is balanced by various microphysical sources of rain, snow and graupel as well as advection and storage of these hydrometeors:

$$P = Q_{LAUT} + Q_{LACC} + Q_{IAUT} + Q_{IACC} + Q_{RIM} + Q_{DEP} + Q_{SUB} + Q_{ADV} - Q_{STOR}. \quad (1)$$

Here, the sources of hydrometeor mass include microphysical processes, such as autoconversion of cloud liquid (LAUT), accretion of cloud liquid (LACC), autoconversion of cloud ice (IAUT), accretion of cloud ice (IACC), riming of cloud liquid (RIM), vapor deposition onto ice (DEP), sublimation of ice (SUB), along with those associated with moisture flux convergence (labeled ADV for advection) and storage (STOR). The storage term is negative because increases in hydrometeors in the domain over time come at the expense of surface precipitation. Each of these terms are integrated over the duration of the simulations and over the domain or a subset of the domain in the horizontal direction and then normalized by the mountain half-width (20 km). Note that, because the Thompson microphysical scheme produces little cloud ice, much of the vapor deposition onto ice phase hydrometeors that occurs in the domain contributes directly to snow growth. Other microphysical schemes would likely have stronger vapor deposition onto cloud ice, so that the autoconversion/accretion of cloud ice would be relatively more important and vapor deposition relatively less important. Also, note that the net tendency of vapor deposition (including deposition, sublimation and rain evaporation) has been averaged over the simulation and then partitioned into regions of deposition and sublimation/evaporation according to the sign of the mean tendency.

A similar budget can be written for the mass of the heavy isotopologues, and the isotopic composition of those contributions can be computed from the ratio of the contribution to heavy isotope mass, e.g., $H_2^{18}O$, to that for the standard isotope, $H_2^{16}O$. The $\delta^{18}O$ of hydrometeor mass generated by each process may then be computed as for precipitation itself, $\delta^{18}O_{precip}$.

In Fig. 4, the total precipitation and the contributions of the dominant microphysical processes to precipitation and its isotopic composition are shown in three regions: the peak (x=295–305 km) and the regions upwind and downwind of the peak. In the following, the sources of precipitation in each region are analyzed. Note that the precipitation produced in each region may fall to the surface there or be transported downstream. In Figs. 4b–d, the contribution of each process in each region has been normalized by the total precipitation in the domain for each case. These normalized contributions can be interpreted as weights, which can be applied to the characteristic isotopic composition from each process to determine $\delta^{18}O_{precip}$.

In the upwind region (Fig. 4b), riming of cloud droplets contributes most to the growth of precipitating hydrometeors, with vapor deposition onto ice making the second largest contribution in most cases. The 25 cm^{-3} simulation differs in the importance of autoconversion and accretion of cloud liquid. Riming and autoconversion of cloud liquid both have a direct dependence on the size of cloud droplets and therefore on CDNC. Accretion of cloud liquid may also depend indirectly on CDNC if less rain is generated through autoconversion as CDNC increases. As autoconversion and accretion of cloud liquid fall off with increasing CDNC, the contribution from vapor deposition increases. The isotopic signatures of the liquid processes are more enriched than the vapor deposition by approxi-

mately 4-9‰ (Fig. 4f), and thus the precipitation in the lower CDNC simulations is more enriched than the higher CDNC simulations. Overall, the microphysics explain the decrease in both the accumulated precipitation and the isotopic content of the precipitation as seen in Fig. 3.

Riming of cloud liquid over the mountain peak is the largest source of precipitation in the three regions and itself produces enough hydrometeor mass to account for half of the surface precipitation in all cases except CDNC=25 cm^{-3} (Fig. 4c). Accretion of cloud liquid and vapor deposition onto ice also contribute to precipitation over the peak. Similar to the upwind region, accretion of cloud liquid decreases with increasing CDNC, though more modestly, but riming actually increases. In this region, vapor deposition onto ice is still the most depleted source term. However, the ice produced by vapor deposition is more enriched above the peak than in the upstream region. The average $\delta^{18}O$ differences between the ice produced by riming and vapor deposition over the peak range between 2-4‰ (Fig. 4g). Therefore, the variation in the source terms of precipitation with CDNC over the peak produce little change in the $\delta^{18}O_{precip}$ formed there, in part because the isotopic composition of the sources are more similar.

Precipitation production on the leeward slope derives predominantly from vapor deposition onto ice in addition to relatively small contributions from ice autoconversion and accretion of cloud liquid (Fig. 4d). One significant difference in this downwind region compared to the other two regions, is the presence of a large sink of precipitation mass caused by sublimation and rain evaporation. This pocket of sublimation/evaporation is expected due to subsidence and thus warming of air as it flows over the mountain peak. Though all of the microphysical source terms increase with CDNC in this region, removal

of precipitation due to sublimation/evaporation essentially balances out the source terms, and the accumulated precipitation remains relatively constant in the different simulations (Fig. 3a). The smaller range of the δ^{18}O in the accumulated precipitation can be attributed to the similarity of the source terms in each simulation, except for that due to sublimation/evaporation which becomes more depleted with increasing CDNC.

3.4. Sensitivity to mountain height and temperature

The sensitivity of domain-integrated precipitation amount and its isotopic composition to CDNC changes was also studied for a number of mountain heights (800 m, 1500 m and 3000 m) and two temperature profiles (with T_{sfc} = 0°C and 7°C)[1]. To understand how precipitation and its isotopic content are related across these simulations, Fig. 5 shows their relationship when integrated over the whole domain (Fig. 5a) and over the regions upstream of the peak, over the peak and downstream of the peak (Figs. 5b–d, respectively). These regions are defined as above in section 3.3. As seen in Fig. 5a, the response of total (domain-integrated) precipitation and its isotopic content to CDNC changes — where it exists — is modest in comparison to that due to mountain height and temperature. The only significant response of $\delta^{18}O_{precip}$ to CDNC occurs for small precipitation amounts (<5 mm) in the upwind region of W800m (Fig. 5b). Otherwise, the change in isotopic content due to temperature exceeds that due to CDNC by a factor of approximately 10 for the ranges of temperature and CDNC explored here. The weaker sensitivity of precipitation to CDNC changes with increasing precipitation is reminiscent of the work of *Muhlbauer et al.* [2010] for mixed-phase clouds and *Miltenberger et al.* [2015] for warm clouds. The possibility remains that a model setup that yields weaker precipitation might show a stronger sensitivity of precipitation to CDNC changes, as in

Miltenberger et al. [2015]. However, the change in $\delta^{18}O_{precip}$ due to CDNC is unlikely to increase far beyond the range seen in the reference case (W800m).

Since the response to CDNC is weak in many cases, the present section focuses on a single CDNC value (200 cm^{-3}) across the range of mountain heights and temperatures to understand the responses to mountain height and temperature seen in Fig. 5. The changing configuration of the orographic cloud with mountain height and temperature is shown in Fig. 6. The orographic cloud produced in the C800m experiment is quite similar to that of the reference simulation in terms of vertical extent (Fig. 6d). However, the extent of the cloud and snow on the lee slope changes with cloud liquid ending closer to the peak and the cloud ice/snow reaching farther down the slope. For the higher mountain heights (Figs. 6b-c, e-f), the liquid cloud is shallower in the colder simulations while the snow has a similar vertical extent. These higher mountain heights also produce more ice/snow than the reference simulation, and in the cold temperature experiments, there is more cloud ice/snow than liquid. Note that the 3000 m mountain wave response depends on temperature, with the isotherms downstream of the mountain suggesting a stronger downslope flow in the colder simulation.

Fig. 7 shows the isotopic composition of water vapor, cloud liquid and combined cloud ice/snow for the three mountain heights with the colder temperature profile ($T_{sfc} = 0°C$). Unlike in the reference simulation, these simulations have little rain, and its isotopic composition is not shown. As noted in section 2.3, the water vapor at the surface upwind of the mountain (Figs. 7a–c) is 8‰ more depleted than that of the reference simulation (Fig. 2a). The water vapor isotopic composition becomes increasingly asymmetric for the higher mountains due to rainout [*Smith et al.*, 2005], and the thin layer of downslope

flow is visible in the water vapor isotopic composition for the 3000 m mountain (Fig. 7c). The cloud liquid is almost entirely confined to the upstream side of the mountain, and its isotopic content (Figs. 7d–f) is tied to the water vapor through the assumption of vapor-liquid isotopic equilibrium. The combined cloud ice/snow (Figs. 7g–i) is more depleted than cloud liquid at the same altitude, and this difference increases with mountain height. On the lee side of the mountain, the snow reaches to the base of the mountain in each case and becomes more depleted with mountain height, as the snow has formed from vapor that either originates at higher altitudes or has been depleted through precipitation.

As suggested by the sensitivity of total precipitation shown in Fig. 5, the distribution of precipitation and its isotopic content across the mountain changes much more substantially with mountain height and temperature than with CDNC (Fig. 8). The precipitation amount increases and shifts upstream with increasing mountain height, and $\delta^{18}O_{precip}$ on the lee slope becomes more depleted with mountain height in agreement with the snow isotopic composition shown in Figs. 7g–i. The lee slope difference in $\delta^{18}O_{precip}$ between the 800 m and 3000 m mountain heights at x=315 km reaches 11‰ and 13‰ in the warm and cold simulations, respectively. Similar differences are seen in the precipitation integrated in the lee of the peak in Fig. 5d. The stronger dependence of $\delta^{18}O_{precip}$ on mountain height in the cold simulations mirrors that seen in total precipitation and its isotopic content in Fig. 5 and suggests that the isotopic lapse rate, the change in $\delta^{18}O_{precip}$ with altitude, itself depends on temperature.

As in section 3.3, the relative contributions of different microphysical pathways to the formation of precipitating hydrometeors are shown in Fig. 9b to understand better the influence of mountain height and temperature on isotopic composition, which was seen

in Fig. 5. Most of the precipitation occurs windward of the peak in the sensitivity simulations, and thus the source terms plotted in Fig. 9b are similar to the breakdown of upwind precipitation. A supplemental Fig. S2 shows the full breakdown of precipitation sources by region as in Fig. 4.

The $\delta^{18}O_{precip}$ is the most enriched in the reference simulation (W800m) compared to all other simulations (Fig. 9c), and this is also the case where the sources of riming and accretion are largest and vapor deposition smallest. The contribution to precipitation from riming decreases with increasing mountain height and decreasing temperature (Fig. 9b), while the contribution of vapor deposition increases. Note that these contributions are normalized by total precipitation, which itself increases with mountain height. While there is considerable variation in the isotopic composition of the precipitation sources with mountain height and temperature, this variation is systematic in the most important contributors to precipitation: riming, vapor deposition and sublimation. As the mountain height increases or the temperature falls, these processes form precipitating hydrometeors from more depleted water vapor in the drier air found at colder temperatures and/or further aloft. Despite the variation with mountain height and temperature seen in Fig. 9d, a clear separation exists between the isotopic compositions contributed by riming and vapor deposition to precipitation, and the shift towards the formation of snow by vapor deposition at colder temperatures and higher mountains is reflected in the more depleted isotopic compositions in those experiments.

It is evident, particularly in the cold temperature experiments, that precipitation source significantly influences the $\delta^{18}O_{precip}$ signal, and that the decreasing $\delta^{18}O_{precip}$ signal with increasing mountain height is not a simple reflection of temperature. The solid line

in Fig. 5a–b represents the regression of the warm temperature experiments' domain-integrated precipitation and $\delta^{18}O_{precip}$. The dashed line in Figs. 5a–b is the same as the solid line, but shifted down by 8‰, which represents the surface vapor $\delta^{18}O$ difference between the warm and cold temperature profiles (see Figs. 2a and 7a). The cold 800 m simulations fall on this dashed line in Fig. 5, but as the mountain height increases, the $\delta^{18}O_{precip}$ values of the cold temperature simulations fall well below this line, implying that precipitation is more depleted than what is expected from the 8‰ offset in the upwind sounding in the cold 1500 m and 3000 m experiments. As noted above, this suggests that the dependence of $\delta^{18}O_{precip}$ on altitude is itself a function of temperature. This can be explained by the combination of three effects. First, the changing sources of precipitation also contribute with a shift from riming to vapor deposition with decreasing temperature. For the C3000m case, the domain-averaged $\delta^{18}O_{precip}$ is close to the $\delta^{18}O$ signatures of vapor deposition itself. Second, the nonlinearity in the relationship between isotopic composition and height plays a role here, as the gap between $\delta^{18}O$ for the warm and cold simulations increases with height due to the curvature of the Rayleigh curve (Fig. S1). Last, the changing structure of the mountain wave with mountain height and temperature may also impact the distribution of precipitation and also its isotopic composition.

4. Discussion and Conclusions

Orographic precipitation is an important water resource, and in this work we have attempted to provide new perspective on how different atmospheric regimes may influence the formation of precipitation. The isotopic composition of orographic precipitation also provides additional information about the sources of water vapor and the microphysical processes that produce this precipitation. In the present study, the microphysical controls

on the isotopic composition of wintertime orographic precipitation have been explored in idealized simulations of flow over a two-dimensional mountain using an isotope-enabled version of WRF. One reference simulation was performed along with sensitivity experiments that varied CDNC, temperature and mountain height to study the responses in the microphysical processes, their respective isotopic composition and the $\delta^{18}O_{precip}$.

One of the main goals of this work has been to study the isotopic signatures of precipitation and cloud microphysical processes and determine if there is a distinct isotopic signal associated with those processes. With an idealized setup using different mountain heights, warm and cold temperature profiles, and increasing CDNC, our simulations show that there is a distinct difference in the $\delta^{18}O$ signatures of microphysical processes. The $\delta^{18}O_{precip}$ reflects the relative contributions from each of the sources, and thus hydrometeors that form from isotopically lighter sources lead to more depleted precipitation. In all of the simulations, precipitation grows mainly by riming of cloud liquid, vapor deposition onto ice, or a combination of the two processes. The $\delta^{18}O$ difference between riming and vapor deposition ranges between 3-8‰ in all simulations and is independent of the environmental temperature. The distinct isotopic signals of the two sources persist despite wide variation in the isotopic composition of these sources with mountain height and temperature. This difference is related mainly to the altitude of the growth processes within the cloud, as vapor deposition occurs both near the surface and in air with more depleted water vapor aloft, and riming predominately happens near the mountain surface.

The sensitivity of $\delta^{18}O_{precip}$ to mountain height and temperature reflects, in part, the changing sources of precipitating hydrometeors. The dominant source of precipitation shifts from riming for smaller mountains and the warmer temperature profile to vapor

deposition for higher mountains and colder temperatures. The more depleted isotopic composition of the precipitating hydrometeors generated by vapor deposition contributes to the decrease of $\delta^{18}O_{precip}$ with mountain height and temperature. It is notable that the relationship between precipitation amount and $\delta^{18}O_{precip}$ driven by increasing mountain height differs with temperature, and that the difference in $\delta^{18}O_{precip}$ between the warm and cold simulations increases with mountain height. This suggests that the isotopic lapse rate is itself a function of temperature, and that this temperature dependence partly results in a shift in the microphysical pathways through which precipitating hydrometeors grow. Additional factors that could also contribute to the temperature dependence of the isotopic lapse rate include the nonlinearity of the Rayleigh curve and changes in the patterns of airflow over the mountain.

We have attempted to illuminate how $\delta^{18}O_{precip}$ depends on the processes responsible for the growth of precipitating hydrometeors. The decrease in $\delta^{18}O_{precip}$ with increasing mountain height and colder temperature profiles is largely driven by the formation of hydrometeors from more depleted water vapor in the drier air further aloft or at colder temperatures. However, the pathways through which precipitating hydrometeors are formed also plays a role, as the more enriched precipitating hydrometers produced by riming contribute less to surface precipitation and the more depleted hydrometeors produced by vapor deposition onto ice contribute more. The weaker dependence of $\delta^{18}O_{precip}$ on CDNC, where it exists, can be explained in a similar manner. While the weak dependence on CDNC suggests a similarly weak dependence on aerosol concentrations, the domain-integrated signal in the strongest case is roughly equivalent to a 1°C shift in temperature along the Rayleigh curve. Such a change might be visible in paleoclimate records of pre-

cipitation if there were systematic shifts in aerosol concentrations on longer timescales. However, if the majority of precipitation was produced in colder conditions, the sensitivity to CDNC might not be visible, as is the case in the more strongly precipitating cases here. While not considered here, mixed-phase orographic precipitation does respond to changes in ice nuclei concentrations [e.g., *Fan et al.*, 2014], and the associated shifts in microphysical processes could also impact the isotopic composition of precipitation.

The results have potential implications for research and field campaigns looking to study the influence of different atmospheric regimes on orographic precipitation, such as IFRACS (a 2014 campaign led by Doug Lowenthal, Gannet Haller and colleagues at the Desert Research Institute: `https://www.eol.ucar.edu/field_projects/ifracs`), ISPA-III [*Ward and Cotton*, 2011] and StormVEx [*Mace et al.*, 2010]. As liquid processes are most responsive to CDNC, locations where precipitation primarily forms through accretion of cloud liquid and/or riming are likely to experience decreased accumulation, a shift in the location of, and a decrease in the $\delta^{18}O_{precip}$. However, the sensitivity depends on both the mountain height and the region above the mountain surface in which precipitation forms and grows. The model could be beneficial to those planning observational campaigns in terms of choosing locations to collect samples. For example, those interested in studying the influence of aerosols on snowfall could identify the regions where precipitation is likely to be most sensitive or least sensitive to aerosol loading.

In this idealized modeling study, we were able to distinguish isotopic signatures of the microphysical growth processes. As the climatology will vary between locations or even seasonally at one location, the model can be used to identify the isotopic signatures of microphysical processes in specific locations, which would help to determine growth

pathways of measured precipitation. The next steps are to use the isotope-enabled microphysics scheme in a realistic setting to study snowfall events at Storm Peak Lab in Colorado observed during the Isotopic Fractionation in Snow (IFRACS) campaign. In this future work, we hope to expand upon our current research by studying the isotopic signatures of the microphysical growth processes that produce the observed precipitation.

Appendix A: Incorporating Isotopologues Into the Microphysics

Stable water isotopologues were added to the Thompson microphysics scheme in the WRF model by duplicating all microphysical processes (e.g., freezing, melting, vapor deposition, evaporation) with additional process rates for the water isotopologues following *Blossey et al.* [2010, App. B]. Except for the sublimation of ice, which is assumed to be non-fractionating, all exchanges between vapor and condensate involve fractionation. The fractionation/equilibration of water isotopologues from rain is included, along with the fractionation of water vapor as it is deposited onto ice phase hydrometeors. Water vapor and cloud liquid are assumed to be in isotopic equilibrium. While a detailed description of the isotopic treatment including all of these processes can be found in appendix B of *Blossey et al.* [2010], we give a brief summary below that emphasizes those processes that play important roles in the cold and mixed-phase clouds central to this study.

For most processes, especially those in which whole hydrometeors are moved from one microphysical category to another (e.g., freezing of cloud droplets to form ice), the heavy isotopologues of water are transferred in proportion to their concentration in the source hydrometeor. For example, the freezing of cloud liquid droplets (wfz) to form cloud ice transfers heavy isotopologues to cloud ice as follows:

$$\left.\frac{dr_i'}{dt}\right|_{wfz} = \left.\frac{dr_i}{dt}\right|_{wfz} \mathcal{R}_c \tag{A1}$$

where $\mathcal{R}_c = r_c'/r_c$ is the isotopic ratio of cloud liquid, and r_c and r_i are the mass mixing ratios of cloud liquid and cloud ice, respectively. The mass mixing ratios of heavy isotopologues are denoted with primes, e.g. r_c'. Further, it is assumed that the isotopic ratio is uniform in each hydrometeor category, so that large and small raindrops have the same isotopic composition, for example. The latter assumption will not hold exactly in reality

and is a source of error; the computation complexity of allowing such variation in a bulk scheme could be considerable.

For the few microphysical processes that result in fractionation (the unequal transfer of heavy and light isotopologues between phases), those processes are represented as described in *Blossey et al.* [2010, App. B]. In general, the lower vibrational energy of the heavier isotopologues of water cause them to prefer the condensed phases (liquid, ice) to the vapor phase, so that their concentrations in vapor are smaller than in the condensed phases. When comparing concentrations of isotopologues, the words "heavier" or "more enriched" are used to describe concentrations of heavy isotopologues that are higher, while "lighter" or "more depleted" are used for smaller concentrations of heavy isotopologues. We supply here a summary of how these processes might affect the isotopic composition of water in mixed-phase clouds.

The efficient exchange between small liquid water droplets in clouds and the surrounding water vapor leads many microphysical schemes (including Thompson) to assume that in-cloud water vapor mixing ratios are equal to the saturation mixing ratio when cloud liquid is present. The complementary condition for heavy isotopologues is that the isotopic ratios of cloud liquid and water vapor are in isotopic equilibrium:

$$\mathcal{R}_c = \alpha_l \, \mathcal{R}_v \tag{A2}$$

where $\mathcal{R}_v$ is the isotopic ratio of water vapor and α_l is the equilibrium fractionation coefficient for liquid [*Majoube*, 1971]. As the equilibration time for isotopic composition of small liquid water droplets is on the order of a few seconds [*Ciais and Jouzel*, 1994], this is in general a good assumption and is included in our implementation.

Given the potentially large supersaturation with respect to ice, we need to consider the non-equilibrium processes driven by gradients of water vapor between the environment and ice particles which leads to vapor deposition onto those particles. The relatively smaller diffusivities of the heavy isotopologues modifies the transfer of water to the particle surface, so that the deposition of heavy isotopologues may be written as

$$\frac{dr_i'}{dt}_{dep} = \alpha_s \alpha_k \mathcal{R}_v \frac{dr_i}{dt}_{dep} \tag{A3}$$

[*Ciais and Jouzel*, 1994], where α_s is the equilibrium fractionation coefficient for ice [*Majoube*, 1970; *Merlivat and Nief*, 1967] and the kinetic fractionation coefficient, α_k, represents the effects of the relative diffusion of the heavy and light isotopologues [*Jouzel and Merlivat*, 1984].

The effects of these two processes on the isotopic composition of liquid and ice in mixed-phase clouds is depicted in Fig. A1. Here, the variation in the saturation ratios with respect to liquid and ice is depicted in the left panel as a function of temperature. In keeping with the assumption in the microphysical scheme, the saturation ratio with respect to liquid is one, while the ice saturation ratio grows with decreasing temperature. The isotopic content of the vapor, cloud liquid and ice formed through vapor deposition is shown in the right panel. Equations A2 and A3 have been used to compute isotopic composition, except for cloud liquid water, whose value is fixed to the relationship observed in mixed-phase orographic clouds by *Lowenthal et al.* [2011],

$$\delta^{18}\mathrm{O}_c = 0.9T - 10.12 \tag{A4}$$

where T is temperature in degrees Celsius. While ice formed through vapor deposition is more enriched than cloud liquid at the same temperature, close to 0°C, increasing the

supersaturation with respect to ice and decreasing temperature causes a stronger kinetic effect during deposition onto cloud ice. Note that vapor deposition onto ice in a liquid class is most efficient at colder temperatures, peaking close to -15°C [*Rogers and Yau*, 1989, p. 161]. As a result, the typical isotopic composition of ice formed through vapor deposition is often more depleted than that of cloud liquid closer to 0°C. Note that these relationships will not hold once the liquid water is removed and the cloud is fully glaciated.

Acknowledgments. This research was partially supported by NSF grants AGS-1062016, AGS-1260368, AGS-1260380, NASA grant NNX13AN47G, and the Joint Institute for the Study of the Atmosphere and Ocean (JISAO) under NOAA Cooperative Agreement NA10OAR4320148, Contribution No. 2416. The Harvard Odyssey cluster provided much of the computing resources for this study. We thank our reviewers for their time and dedication. Their guidance and suggestions have greatly helped in the presentation of this work. All data for this paper is properly cited and referred to in the reference list. Those interested in the isotope-enabled Thompson microphysics scheme should contact co-author Peter Blossey (pblossey@uw.edu).

Notes

1. Each simulation is labeled according to its temperature and mountain height. For example, W800m denotes the reference case with "W" denoting the warmer sounding with $T_{sfc} = 7°C$ and, in other runs, "C" the colder sounding with $T_{sfc} = 0°C$.

References

Albrecht, B. A. (1989), Aerosols, cloud microphysics, and fractional cloudiness, *Science*, *47*, 1227-1230.

Anderson, L., M. Berkelhammer, and M. A. Mast (2015), Isotopes in North American Rocky Mountain snowpack 1993-2014, *Quat. Sci. Rev.*, doi:10.1016/j.quascirev.2015.03.023.

Blossey, P. N., Z. Kuang, and D. M. Romps (2010), Isotopic composition of water in the tropical tropopause layer in cloud-resolving simulations of an idealized tropical circulation, *J. Geophys. Res.*, *115*, D24309.

Bony, S., C. Risi, and F. Vimeux (2008), Influence of convective processes on the isotopic composition (δ^{18}O and δD) of precipitation and water vapor in the tropics: 1. Radiative- convective equilibrium and Tropical Ocean-Global Atmosphere-Coupled Ocean-Atmosphere Response Experiment (TOGA-COARE), *J. Geophys. Res.*, *113*(D19), 1-21.

Borys, Randolph D., D. H. Lowenthal, and D. L. Mitchell (2000), The relationships among cloud microphysics, chemistry, and precipitation rate in cold mountain clouds, *Atmos. Environ.*, *34*(12), 2593-2602.

Borys, Randolph D., D. H. Lowenthal, D. H. Cohn and W. O. J. Brown (2003), Mountaintop and radar measurements of anthropogenic aerosol effects on snow growth and snowfall rate, *Geophys. Res. Lett.*, *30*(10).

Ciais, P. and J. Jouzel (1994), Deuterium and oxygen 18 in precipitation: Isotopic model, including mixed cloud processes, *J. Geophys. Res. Atmos.*, *99*(D8), 16793-16803.

Clark, I. D. and P. Fritz (1997),Environmental isotopes in hydrogeology, CRC press.

Colle, B. A. (2004), Sensitivity of orographic precipitation to changing ambient conditions and terrain geometries: An idealized modeling perspective, *J. Atmos. Sci.*, *61*, 588-606.

722 Conroy, J. L., K. M. Cobb and D. Noone (2013), Comparison of precipitation isotope
723 variability across the tropical Pacific in observations and SWING2 model simulations,
724 *J. Geophys. Res.*, *118*, 5867–5892, doi:10.1002/jgrd.50412.

725 Coplen, T. P., P. J. Neiman, A. B. White and F. M. Ralph (2015), Categorisation of
726 northern California rainfall for periods with and without a radar brightband using
727 stable isotopes and a novel automated precipitation collector, *Tellus B*, *67*, 28574,
728 doi:10.3402/tellusb.v67.28574.

729 Creamean, J. M., A. P. Ault, A. b. White, P. J. Neiman, F. M. Ralph, P. Minnis, and
730 K. A. Prather (2015), Impact of interannual variationsin aerosol particle sources on
731 orographic precipitation over California's Central Sierra Nevada, *Atmos. Chem. Phys.*
732 *Discuss.*, *15*, 931-964.

733 Dansgaard,W. (1952), Use of stable isotopes in biological research, *Ugeskrift for laeger*,
734 *114*(36), 1209-1213.

735 Dansgaard,W. (1964), Stable isotopes in precipitation, *Tellus*, *16*, 436-468.

736 Demoz, B.B., J. A. Warburton and R. H. Stone(1991), The influence of riming on oxygen
737 isotopic composition of ice-phase precipitation, *Atmos. Res.*, *26*, 463-488.

738 Fan, J., L. R. Leung, P. J. DeMott, J. M. Comstock, B. Singh, D. Rosenfeld, J. M.
739 Tomlinson, A. White, K. A. Prather, P. Minnis, J. K. Ayers, and Q. Min (2014),
740 Aerosol impacts on California winter clouds and precipitation during CalWater 2011:
741 local pollution versus long-range transported dust, *Atmos. Chem. Phys.*, *14*, 81–101,
742 doi:10.5194/acp-14-81-2014.

743 Field, R. D. (2010),Observed and modeled controls on precipitation δ^{18}O over Europe:
744 From local temperature to the Northern Annular Mode, *J. Geophys. Res.*, *115*, D12101,

745 doi:10.1029/2008JD013370.

746 Galewsky, J. (2008), Orographic clouds in terrain-blocked flows: An idealized modeling
747 study, *J. Atmos. Sci.*, *65*, 3460-3478.

748 Galewsky, J. (2009), Orographic precipitation isotopic ratios in stratified atmospheric
749 flows: Implications for paleoelevation studies, *Geology*, *37*(9), 791-794.

750 Hobbs, P. V. (1975), The nature of winter clouds and precipitation in the Cascade Moun-
751 tains and their modification by artificial seeding. Part I: Natural conditions, *J. Appl.*
752 *Meteor.*, *14*, 783-804.

753 Jirak, I. L. and W. R. Cotton (2006), Effect of air pollution on precipitation along the
754 Front Range of the Rocky Mountains, *J. Appl. Meteor. Climatol*, *45*(1), 236-245.

755 Jouzel, J. (2003), Water Stable Isotopes: Atmospheric Composition and Applications in
756 Polar Ice Core Studies, *Treatise Geochem.*, *4*, 213–243.

757 Jouzel, J. and L. Merlivat (1984), Deuterium and oxygen 18 in precipitation: Modeling
758 of the isotopic effects during snow formation, *J. Geophys. Res. Atmos.*, *89*(D7), 11749-
759 11757.

760 Khain, A., and A. Pokrovsky (2004), Effects of atmospheric aerosols on deep convective
761 clouds as seen from simulations using a spectral microphysics mixed-phase cumulus
762 cloud model, *J. Atmos. Sci.*, *61*, 2983-3001.

763 Lawrence, J. R., S. D. Gedzelman, X. Zhang, and R. Arnold (1998),Stable isotope ratios
764 of rain and vapor in 1995 hurricanes, *J. Geophys. Res. Atmos.*, *103*(D10), 11381-11400.

765 Lechler, A. R. and J. Galewsky (2013), Refining paleoaltimetry reconstructions of the
766 Sierra Nevada, California, using air parcel trajectories. *Geology*, *41*(2), 259–262.

Lee, J. E. I. Fung, D. J. DePaolo, and C. C. Henning (2007), Analysis of the global distribution of water isotopes using the NCAR atmospheric general circulation model, *J. Geophys. Res.*, *112*(D16).

Liu, C., K. Ikeda, G. Thompson, R. Rasmussen and J. Dudhia (2011), High-Resolution Simulations of Wintertime Precipitation in the Colorado Headwaters Region: Sensitivity to Physics Parameterizations. *Mon. Wea. Rev.*, *139*, 3533-3553. doi:10.1175/MWR-D-11-00009.1.

Lohmann, U.(2004), Can anthropogenic aerosols decrease the snowfall rate?, *J. Atmos. Sci.*, *61*, 2457-2468.

Lowenthal, D. H., R. D. Borys, W. Cotton, S. Saleeby, S. A. Cohn and W. O. J. Brown (2011), The altitude of snow growth by riming and vapor deposition in mixed-phase orographic clouds, *Atmos. Environ.*, *45*(2), 519-522.

Lynn, B., A. Khain, D. Rosenfeld, and W. L. Woodley (2007), Effects of aerosols on precipitation from orographic clouds, *J. Geophys. Res.*, *112*, D10225.

Mace, J. and Coauthors (2010), STORMVEX: The Storm Peak Lab Cloud Property Validation Experiment Science and Operations Plan, ARM Technical Report, DOE/SC-ARM-10-021, available at: www.arm.gov.

Majoube, M. (1970), Fractionation factor of 18O between water vapour and ice, *Nature*, 1242-1242.

Majoube, M. (1971), Fractionation of oxygen 18 and of deuterium between water and its vapor, *J. Chem. Phys.*, *68*, 1423-1436.

Merlivat, L. and G. Nief (1967), Isotopic fractionation of solid-vapor and liquid-vapor changes of state of water at temperatures below 0°C, *Tellus*, *19*, 122-127.

Miltenberger, A. K., A. Seifert, H. Joos, and H. Wernli (2015), A scaling relation for warm-phase orographic precipitation - A Lagrangian analysis for 2D mountains, *Quart. J. Roy. Meteorol. Soc.*, doi:10.1002/qj.2514.

Mitchell, D. L., R. Zhang, and R. L. Pitter (1990), Mass dimensional relationships for ice particles and the influence of riming on snowfall rates, *J. Appl. Meteor.*, *29*, 153-163.

Muhlbauer, A. and U. Lohmann (2008), Sensitivity studies of the role of aerosols in warm-phase orographic precipitation in different dynamical flow regimes, *J. Atmos. Sci.*, *65*, 2522-2542.

Muhlbauer, A., T. Hashino, L. Xue, A. Teller, U. Lohmann, R. M. Rasmussen, I. Geresdi, and Z. Pan (2010), Intercomparison of aerosol-cloud-precipitation ineractions in stratiform orographic mixed-phase clouds, *Atmos. Chem. Phys.*, *10*(17), 8173-8196.

Noone, D. and I. Simmonds (2002), Associations between δ18O of Water and Climate Parameters in a Simulation of Atmospheric Circulation for 1979-95*J. Climate*, *15*(22), 3150-3169.

Pfahl, S., H. Wernli, and K. Yoshimura (1999),The isotopic composition of precipitation from a winter storm–a case study with the limited-area model COSMOiso, *Atmos. Chem. Phys.*, *12*(3).

Poage, M. A., and C. P. Chamberlain (2001), Empirical relationships between elevation and the stable isotope composition of precipitation and surface waters: Considerations for studies of paleoelevation change. *American Journal of Science*, *301*, 1-15, doi:10.2475/ajs.301.1.1.

Prein, A. F., W. Langhans, G. Fosser, A. Ferrone, N. Ban, K. Goergen, M. Keller, M. Tölle, O. Gutjahr, F. Feser, et al. (2015), A review on regional convection-permitting

climate modeling: Demonstrations, prospects, and challenges, *Rev. Geophys.*, *53*, 323–361, doi:10.1002/2014RG000475.

Pruppacher, H. and J. Klett (1997), *Microphysics of clouds and precipitation*, 2nd ed. Kluwer Academic Publisher: Dordrecht; 584 pp.

Ramanathan, V., P. J. Crutzen, J. T. Kiehl and D. Rosenfeld (2001), Aerosols, climate and the hydrologic cycle, *Science*, *294*, 2119-2124.

Reinking, R. F., J. B. Snider, and J. L. Coen (2000), Influences of storm-embedded orographic gravity waves on cloud liquid water and precipitation, *J. Appl. Meteor.*, *39*, 733-759.

Risi, C., S. Bony, and F. Vimeux (2008), Influence of convective processes on the isotopic composition (δ^{18}O and δD) of precipitation and water vapor in the tropics: 2. Physical interpretation of the amount effect, *J. Geophys. Res.*, *113*, D19306, doi:10.1029/2008JD009943.

Rogers, R. R. and M. K. Yau (1989), *A short course in cloud physics*, 3rd ed. Butterworth-Heinemann, Woburn, MA, USA. 290 pp.

Rosenfeld, D., J. Dai, X. Yu, Z. Yao, X. Xu, X. Yang, and C. Du (2008), Inverse relations between amounts of air pollution and orographic precipitation, *Science*, *315*, 1396-1398.

Rowley, D. B., R. T. Pierrehumbert, and B. S. Currie (2001). A new approach to stable isotope-based paleoaltimetry: implications for paleoaltimetry and paleohypsometry of the High Himalaya since the Late Miocene. *Earth and Planetary Science Letters*, *188*(1), 253-268.

Saleeby, S. M., and Coauthors (2006), Model aerosol sensitivity studies and microphysical interactions in an orographic snowfall event, *12th Con. on Moun-*

836 *tain Meteorology*, Santa Fe, NM, Amer. Meteor. Soc. 4.4. [Available online at
837 http://ams.confex.com/ams/pdfpapers/126031.pdf]
838 Saleeby, S. M. and W. R. Cotton (2008), A binned approach to cloud-droplet riming
839 implemented in a bulk microphysics model, *J. Appl. Meteor. Climatol.*, *47*(2), 694-703.
840 Saleeby, S. M., W. R. Cotton, D. Lowenthal, R. D. Borys and M. A. Wetzel (2009), In-
841 fluence of cloud condensation nuclei on orographic snowfall, *J. Appl. Meteor. Climatol.*,
842 *48*, 903-922.
843 Saleeby, S. M., W. R. Cotton, and J. D. Fuller (2011), The cumulative impact of cloud
844 droplet nucleating aerosol on orographic snowfall in Colorado, *J. Appl. Meteor. Clima-*
845 *tol.*, *50*, 604-625.
846 Saleeby, S. M., W. R. Cotton, D. Lowenthal, and J. Messina (2013), Aerosol impacts on
847 the microphysical growth processes of orographic snowfall, *J. Appl. Meteor. Climatol.*,
848 *52*, 834-852.
849 Skamarock, W. C. and J. B. Klemp (2008), A time-split non-hydrostatic atmospheric
850 model for weather research and forecasting applications, *J. Comp. Phys.*, *227*, 3465-
851 3485.
852 Smith, R. B., I. Barstad, and L. Bonneau (2005), Orographic precipitation and Oregon's
853 climate transition, *J. Atmos. Sci.*, *62*(1), 177-191.
854 Smith, R. B. and J. P. Evans (2007), Orographic precipitation and water vapor fraction-
855 ation over the southern Andes, *J. Hydrometeor.*, *8*(1), 3-19.
856 Stewart, M. K. (1975), Stable isotope fractionation due to evaporation and isotopic ex-
857 change of falling waterdrops: Applications to atmospheric processes and evaporation of
858 lakes, *J. Geophys. Res.*, *80*(9), 1133-1146.

Thompson, G., P. R. Field, R. M. Rasmussen, and W. D. Hall (2008), Explicit forecasts of winter precipitation using an improved bulk microphysics scheme. Part II: Implementation of a new snow parameterization, *Mon. Wea. Rev.*, *136*, 5095-5115.

Vuille, M., R. S. Bradley, M. Werner, R. Healy, and F. Keimig (2003), Modeling δ^{18}O in precipitation over the tropical Americas: 1. Interannual variability and climatic controls, *J. Geophys. Res.*, *108*, 4174, doi:10.1029/2001JD002038.

Wang, P. K. and W. Ji (2000), Collision efficiencies of ice crystals at low-intermediate Reynolds numbers colliding with supercooled cloud droplets: A numerical study, *J. Atmos. Sci.*, *57*, 1001-1009.

Warburton, J. A. and T. P. DeFelice (1986), Oxygen isotopic composition of central Sierra Nevada precipitation, I. Identification of ice-phase water capture regions in winter storms, *Atmos. Res.*, *20*(1), 11-22.

Warburton, J. A., B. B. Demoz, and R. H. Stone (1993), Oxygen isotopic variations of snowfall from winter storms in the central Sierra Nevada; Relation to ice growth microphysics and mesoscale structure, *Atmos. Res.*, *29*(3), 135-151.

Ward, D. S. and W. R. Cotton (2011), Cold and transition season cloud condensation nuclei measurements in western Colorado, *Atmos. Chem. Phys.*, *11*, 4303-4317.

Xiao, H., Y. Yin, L. Jin, Q. Chen, and J. Chen (2014), Simulation of aerosol effects on orographic clouds and precipitation using WRF model with a detailed bin microphysics scheme, *Atmos. Sci. Lett.*, *15*(2), 134-139.

Zubler, E. M., U. Lohmann, D. Luthi, C. Schar, and A. Muhlbauer (2011), Statistical analysis of aerosol effects on simulated mixed-phased clouds and precipitation in the Alps, *J. Atmos. Sci.*, *68*, 1474-1492.

Figure 1. Contoured temperature (black) and mixing ratios of cloud liquid water (shaded) and combined cloud ice/snow (contoured) for the 800 m warm temperature simulations, averaged over the last four hours of each simulation. Cloud droplet number concentrations of (a) 25 cm^{-3}, (b) 200 cm^{-3}, and (c) 800 cm^{-3} are shown to illustrate sensitivity to CDNC. Units are kg kg^{-1} for hydrometeor mixing ratios and K for temperature.

Figure 2. Average over the last four hours of $\delta^{18}O$ of (a) vapor, (b) rain, (c) cloud liquid and (d) ice/snow for reference simulation with a CDNC of 200 cm^{-3}.

Figure 3. (a) Precipitation accumulated over the 12 hours of the simulation and (b) the associated $\delta^{18}O_{precip}$ for the reference simulation and its sensitivity to CDNC changes. The mountain peak is located at 300 km.

Figure 4. Breakdown of (a) accumulated precipitation in the reference simulation over the whole domain and the regions upwind of the peak, over the peak and downwind of the peak, as well as (e) the respective average $\delta^{18}O$ values. The contributions from precipitation sources normalized by the total, domain-integrated precipitation in the three subregions are shown in (b–d) and the corresponding isotopic signatures in (e–g). The accumulated precipitation and its sources are integrated over the domain and normalized by the mountain half-width (20 km). Sources are: autoconversion of cloud liquid (laut), accretion of cloud liquid by rain (lacc), autoconversion of cloud ice (iaut), riming of cloud liquid (rim), vapor deposition onto ice (dep), and sublimation of ice/evaporation of rain (sub).

Figure 5. Scatter plot of area-integrated precipitation vs $\delta^{18}O_{precip}$ for all mountain heights, temperatures and CDNC values. These quantities are presented both for the whole domain (a) and for regions upstream of the peak (b), over the peak (c) and to the lee of the peak (d). For each experiment, the CDNC value is indicated by the color and size of the symbol, while the mountain height and temperature are shown by the shape of the symbol. The grey solid line in (a) and (b) is the regression of the domain averages in the warm temperature experiments and the dashed line is the solid line shifted down by 8‰. The regression is not shown in (c) and (d) because the isotopic composition over and downwind of the peak depends on the precipitation amount upstream.

Figure 6. As in figure 1, but for the 200 cm^{-3} simulations from the (a) 800 m, (b) 1500 m, (c) 3000 m warm temperature experiments and (d) 800 m, (e) 1500 m, and (f) 3000 m cold temperature experiments.

Figure 7. Based on averages over the last four hours of each simulation, $\delta^{18}O$ of (top) vapor, (middle) cloud liquid and (bottom) ice/snow for the (a,d,g) 800 m, (b,e,h) 1500 m, and (c,f,i) 3000 m cold temperature experiments with a CDNC of 200 cm^{-3}.

Figure 8. Distribution of precipitation accumulated over the 12 hour simulations in (a) warm experiments and (b) cold experiments. Corresponding $\delta^{18}O_{precip}$ for (c) warm experiments and (d) cold experiments. All profiles are based on the 200 cm^{-3} simulations. The mountain peak is located at 300 km. Note that the axis limits for $\delta^{18}O_{precip}$ have been shifted by 8 ‰ from the warm to cold simulations to account for the difference in the isotopic composition of vapor at the surface in the two cases.

Case	CDNC	Total Prec	Snow	Graupel	Rain	Spillover
W800m	25	38.6mm	7.8%	7%	85.2%	37%
W800m	100	32.1mm	13.5%	12.9%	73.6%	59%
W800m	200	28.5mm	14.3%	13.7%	72%	56%
W800m	400	23.7mm	14.8 %	14.2%	70.8%	62%
W800m	800	18.3mm	13.8%	13%	73.1%	68%
C800m	25	34.2mm	92.2%	2.6%	5.2%	45%
C800m	100	32.2mm	96.3%	3%	0.7%	50%
C800m	200	30.9mm	96.9%	2.9%	0.2%	53%
C800m	400	29.3mm	97.5%	2.5%	–	56%
C800m	800	26.6mm	98.1%	1.9%	–	61%
W1500m	25	113.6mm	60.9%	7%	32.1%	31%
W1500m	100	110.5mm	64.1%	11%	24.9%	33%
W1500m	200	106.6mm	65.8%	13%	21.2%	35%
W1500m	400	104.8mm	67%	13.7%	19.3%	36%
W1500m	800	105.3mm	67.1%	14%	18.9%	37%
C1500m	25	91.3mm	96.1%	0.5%	3.4%	32%
C1500m	100	92.6mm	98.3%	0.6%	1.1%	33%
C1500m	200	90.7mm	98.7%	0.7%	0.6%	34%
C1500m	400	91.7 mm	99.1%	0.7%	0.2%	35%
C1500m	800	87.3mm	99.4%	0.6%	–	38%
W3000m	25	235.8mm	67.8%	3.2%	29%	27%
W3000m	100	237.8mm	69.1%	3.8%	27.1%	27%
W3000m	200	233.9mm	71%	4.3%	24.7%	28%
W3000m	400	232.1mm	72.1%	4.8%	23.1%	29%
W3000m	800	227.9mm	74%	5.3%	20.7%	31%
C3000m	25	182.3mm	97.3%	0.5%	2.2%	20%
C3000m	100	183.2mm	98.7%	0.3%	1%	21%
C3000m	200	166.7mm	99%	0.3%	0.7%	22%
C3000m	400	175.1mm	99.4%	0.3%	0.3%	22%
C3000m	800	172.2mm	99.6%	0.3%	0.03%	22%

Table 1: Breakdown of the major statistics for all runs. Columns indicate the case (height and cold (C) or warm (W) initial temperature profile), cloud droplet number concentration (CDNC) in cm^{-3}, normalized (by the mountain half-width) domain-integrated precipitation over 12 hour simulation, and the percent of snow, graupel and rain. Spillover is the ratio of the total leeward precipitation to the total mountain precipitation.

Figure 9. Breakdown of (a) total precipitation, snow and graupel and (c) corresponding δ^{18}O values for all experiments. The contributions from (b) precipitation sources normalized by the total precipitation and (d) the corresponding isotopic signatures for all experiments. Sources from left to right are: autoconversion of cloud liquid (LAUT), accretion of cloud liquid by rain (LACC), autoconversion of cloud ice (IAUT), accretion of cloud ice (IACC), riming of cloud liquid (RIM), vapor deposition onto ice (DEP), and sublimation of ice/evaporation of rain (SUB). All values are based on the 200 cm^{-3} simulations.

Figure A1. [Left panel:] the saturation ratios with respect to cloud liquid (blue) and ice (green) as a function of temperature. [Right panel:] δ^{18}O of in-cloud water vapor (black), cloud liquid (blue) and vapor deposition onto ice particles (green) as a function of temperature.

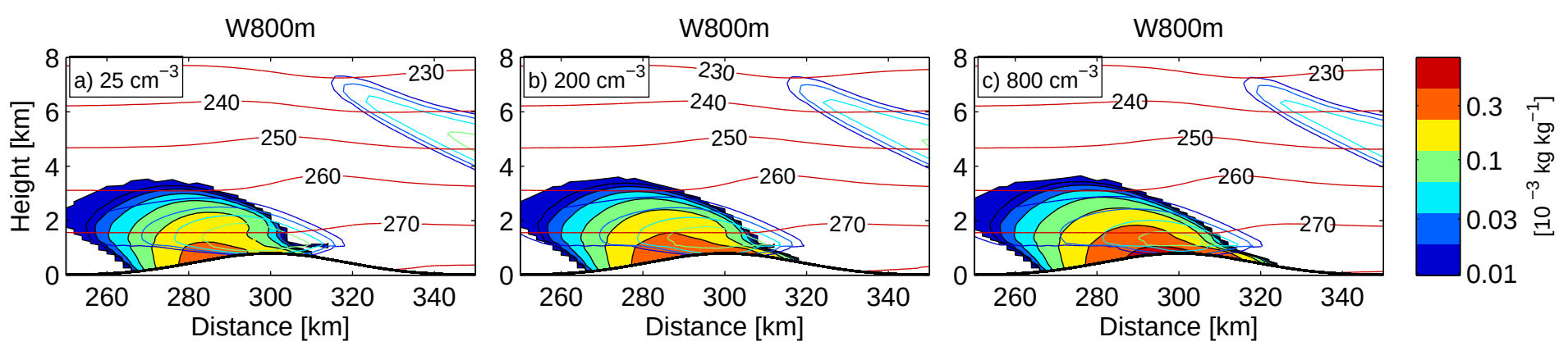
W800m
a) 25 cm^{-3}
b) 200 cm^{-3}
c) 800 cm^{-3}
230
240
250
260
270
Height [km]
0
2
4
6
8
260
280
300
320
340
Distance [km]
0.3
0.1
0.03
0.01
[10^{-3} kg kg^{-1}]

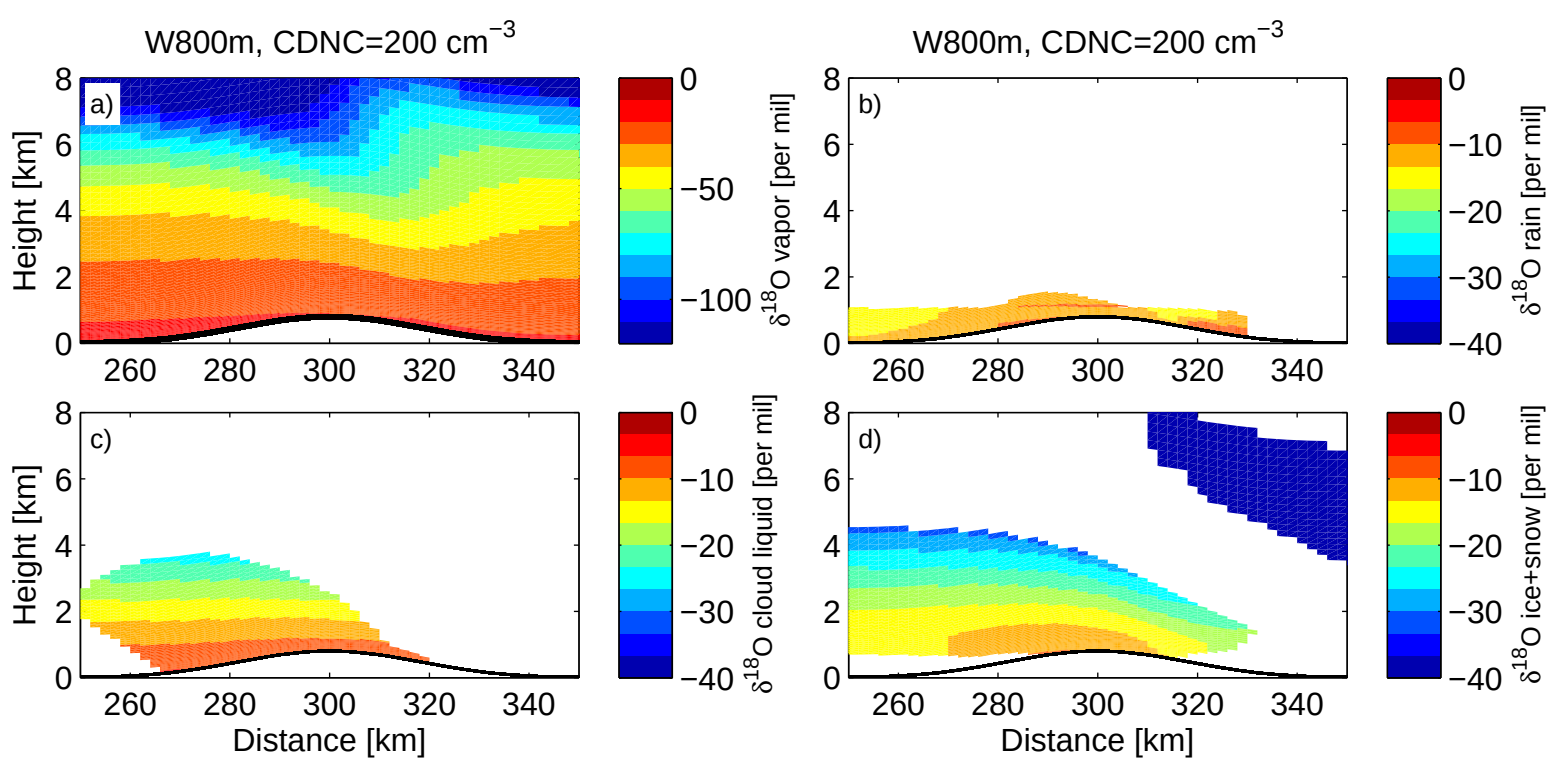
W800m, CDNC=200 cm^{-3}
W800m, CDNC=200 cm^{-3}
a)
b)
c)
d)
Height [km]
Distance [km]
δ^{18}O vapor [per mil]
δ^{18}O rain [per mil]
δ^{18}O cloud liquid [per mil]
δ^{18}O ice+snow [per mil]

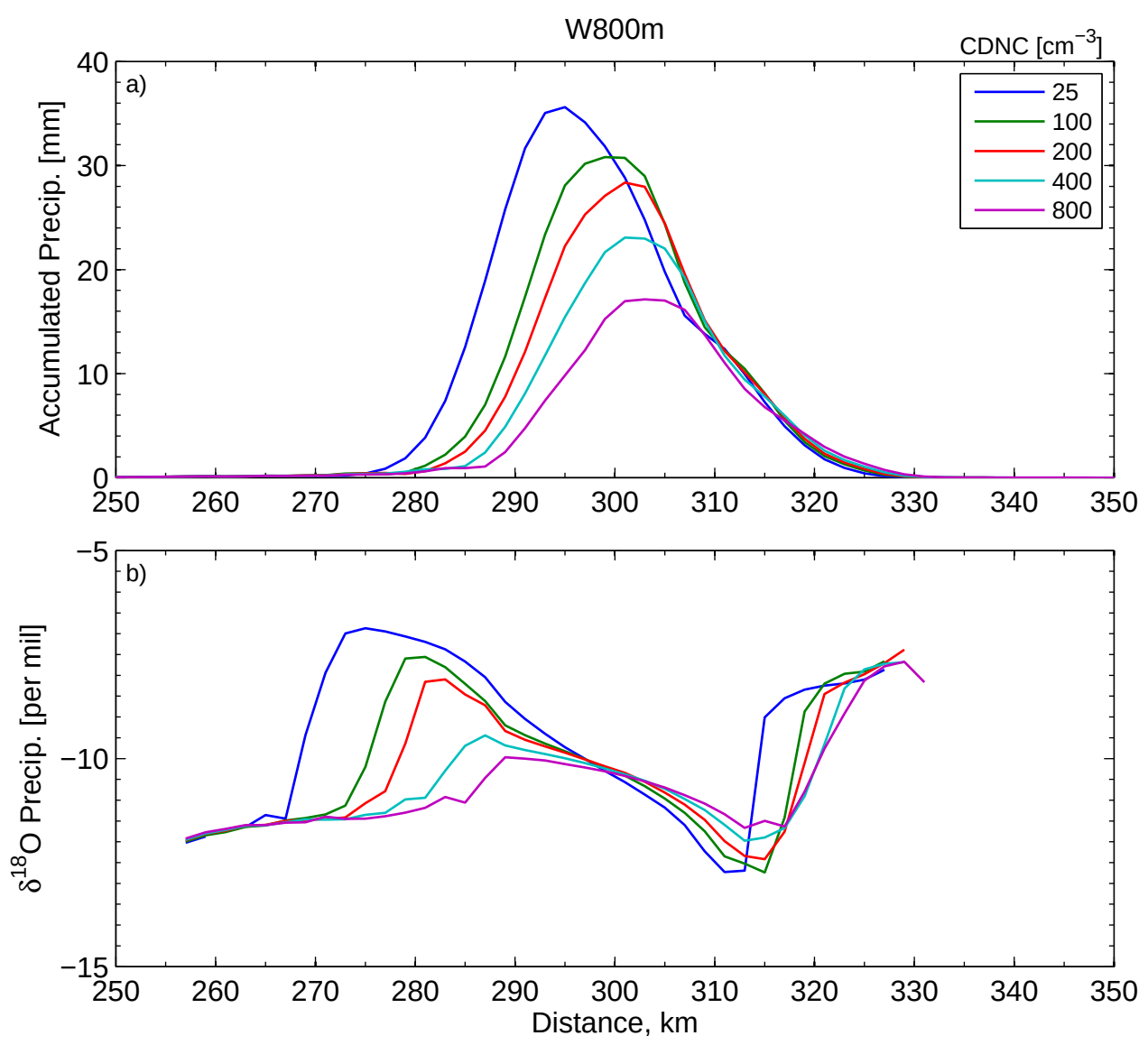
W800m
CDNC [cm^{-3}]
25
100
200
400
800
a)
Accumulated Precip. [mm]
0
10
20
30
40
b)
δ^{18}O Precip. [per mil]
−5
−10
−15
250
260
270
280
290
300
310
320
330
340
350
Distance, km

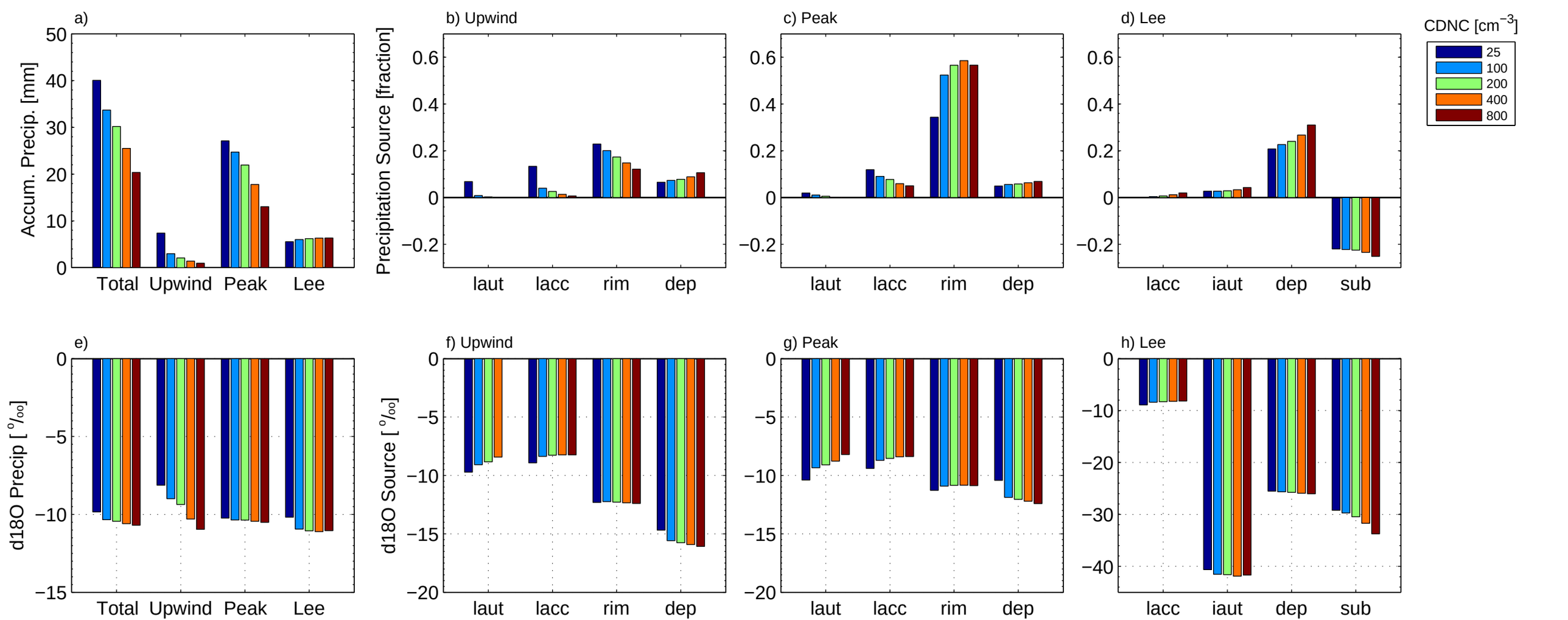
a)
b) Upwind
c) Peak
d) Lee
e)
f) Upwind
g) Peak
h) Lee
Accum. Precip. [mm]
Precipitation Source [fraction]
d18O Precip [°/₀₀]
d18O Source [°/₀₀]
Total
Upwind
Peak
Lee
laut
lacc
rim
dep
iaut
sub
CDNC [cm^{-3}]
25
100
200
400
800

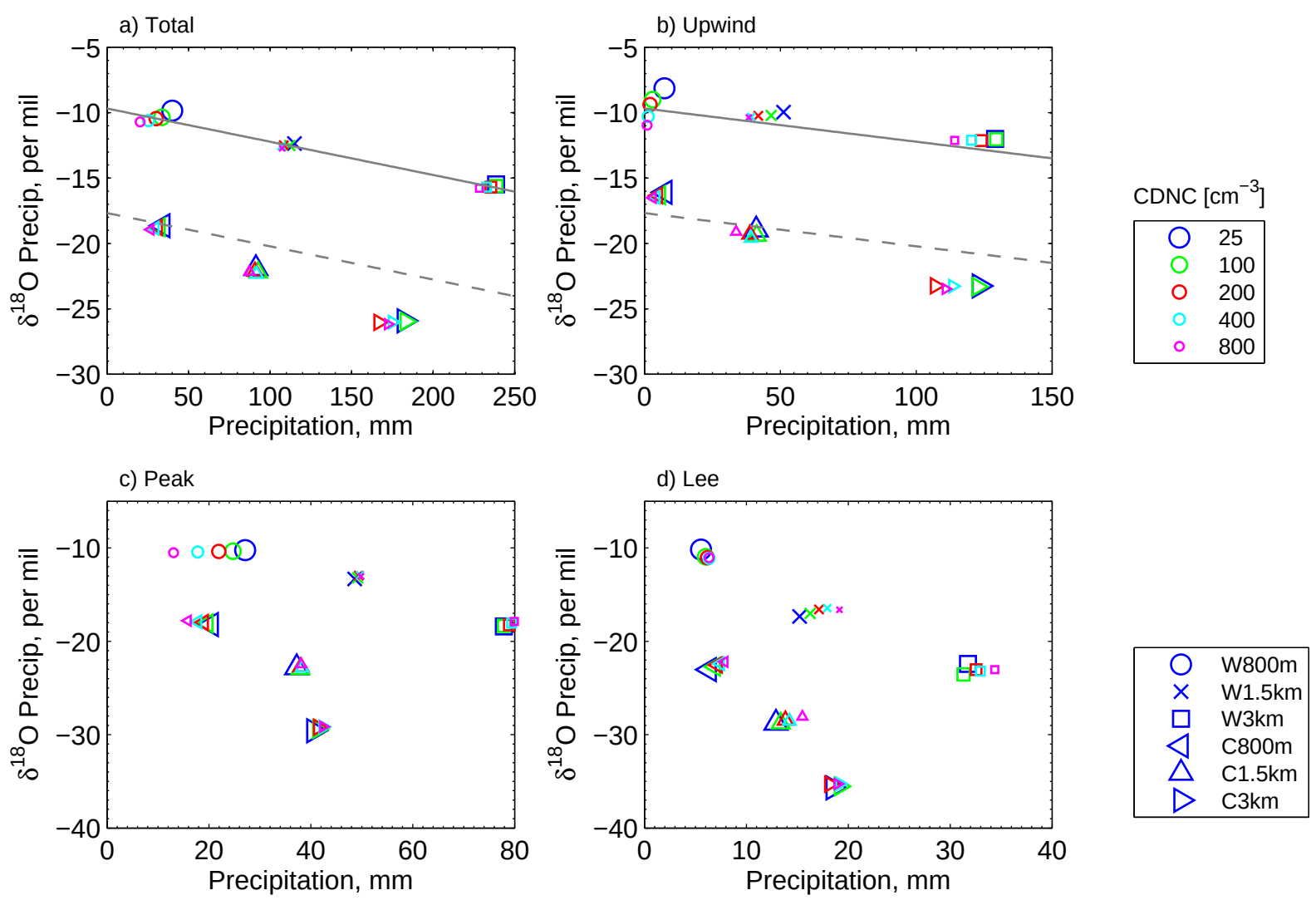
a) Total
b) Upwind
c) Peak
d) Lee
δ18O Precip, per mil
Precipitation, mm
CDNC [cm−3]
25
100
200
400
800
W800m
W1.5km
W3km
C800m
C1.5km
C3km

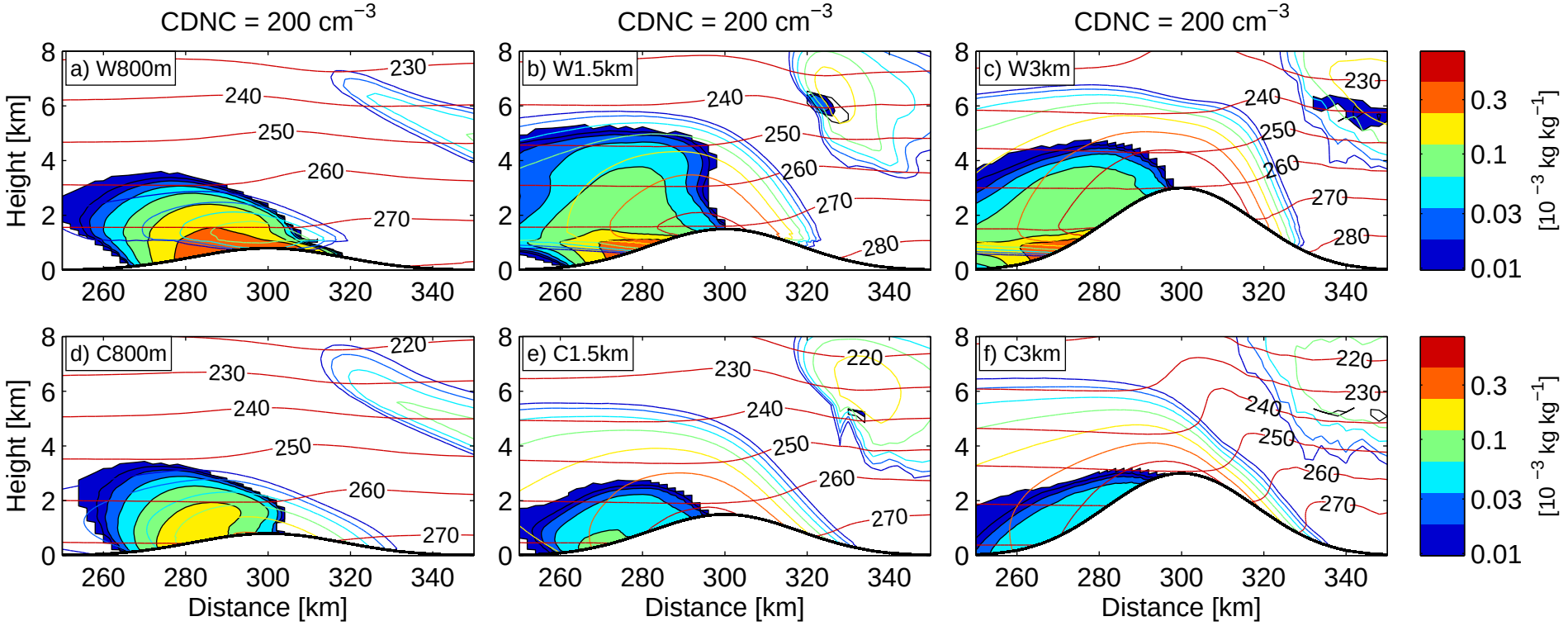
CDNC = 200 cm^{-3}
CDNC = 200 cm^{-3}
CDNC = 200 cm^{-3}
a) W800m
b) W1.5km
c) W3km
d) C800m
e) C1.5km
f) C3km
Height [km]
Height [km]
Distance [km]
Distance [km]
Distance [km]
[10^{-3} kg kg^{-1}]
[10^{-3} kg kg^{-1}]
0.3
0.1
0.03
0.01

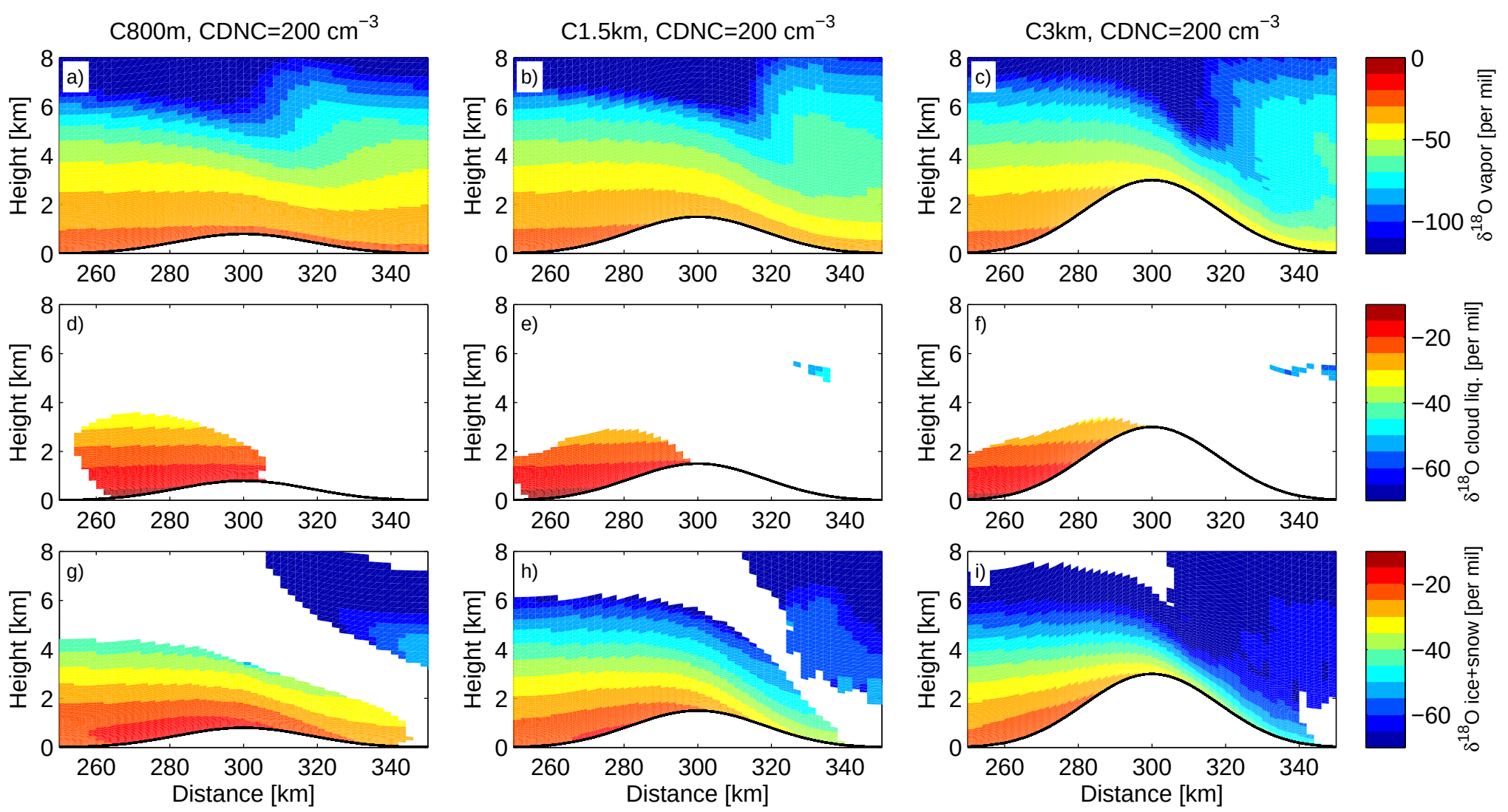
C800m, CDNC=200 cm^{-3}
C1.5km, CDNC=200 cm^{-3}
C3km, CDNC=200 cm^{-3}
a)
b)
c)
d)
e)
f)
g)
h)
i)
Height [km]
Distance [km]
0
2
4
6
8
260
280
300
320
340
0
−50
−100
−20
−40
−60
δ^{18}O vapor [per mil]
δ^{18}O cloud liq. [per mil]
δ^{18}O ice+snow [per mil]

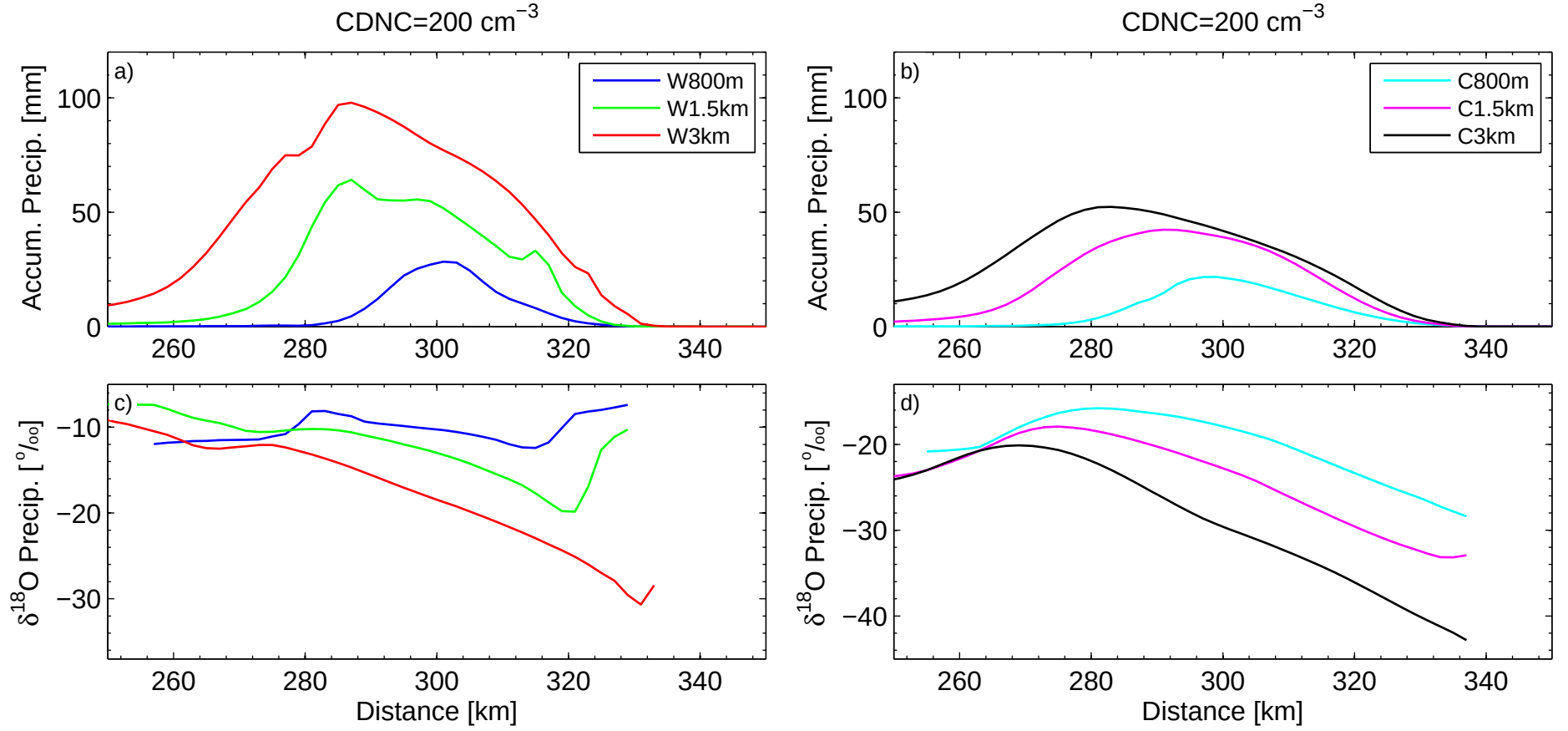
CDNC=200 cm^{-3}
CDNC=200 cm^{-3}
a)
b)
c)
d)
W800m
W1.5km
W3km
C800m
C1.5km
C3km
Accum. Precip. [mm]
δ^{18}O Precip. [‰]
Distance [km]
0
50
100
−10
−20
−30
−40
260
280
300
320
340

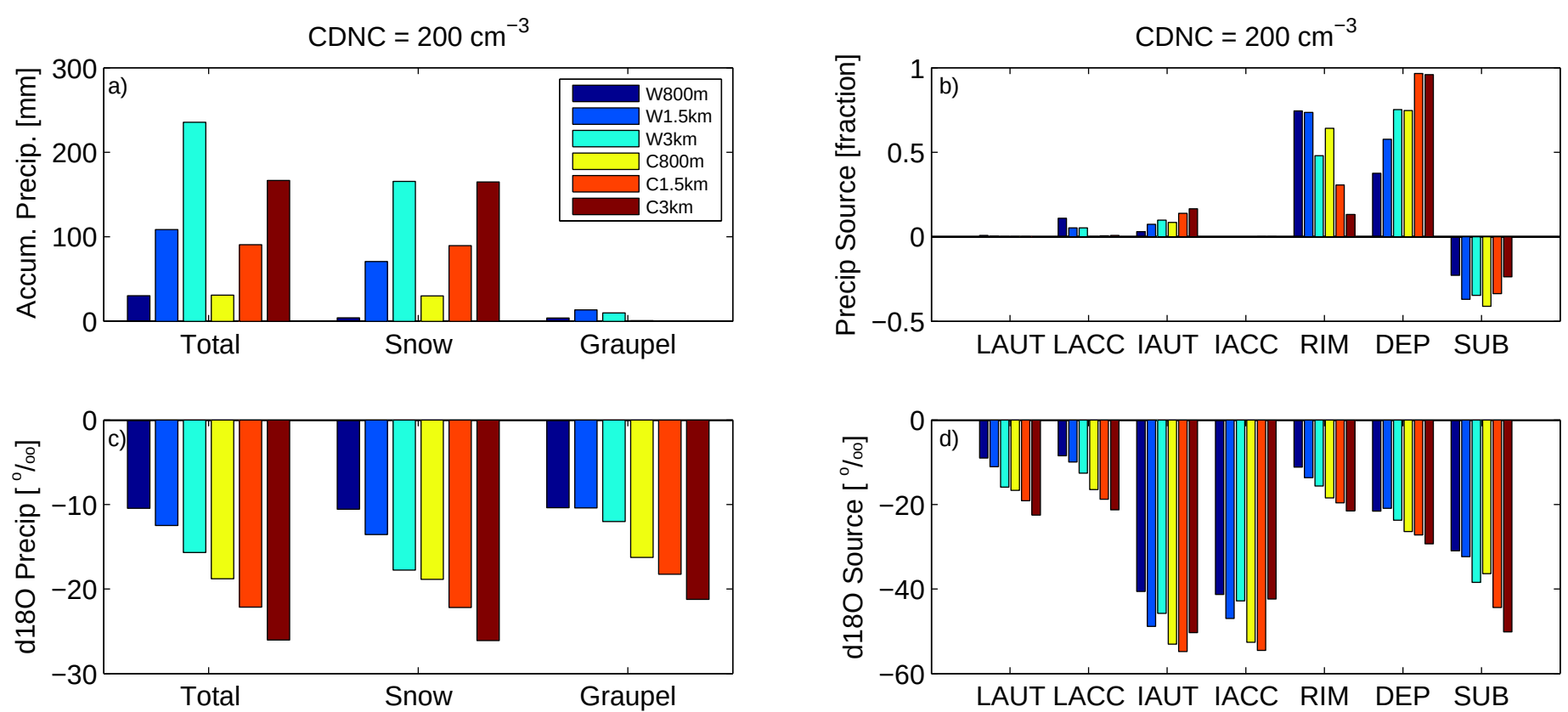
CDNC = 200 cm^{-3}
a)
Accum. Precip. [mm]
300
200
100
0
W800m
W1.5km
W3km
C800m
C1.5km
C3km
Total
Snow
Graupel
CDNC = 200 cm^{-3}
b)
Precip Source [fraction]
1
0.5
0
−0.5
LAUT
LACC
IAUT
IACC
RIM
DEP
SUB
c)
d18O Precip [°/₀₀]
0
−10
−20
−30
Total
Snow
Graupel
d)
d18O Source [°/₀₀]
0
−20
−40
−60
LAUT
LACC
IAUT
IACC
RIM
DEP
SUB

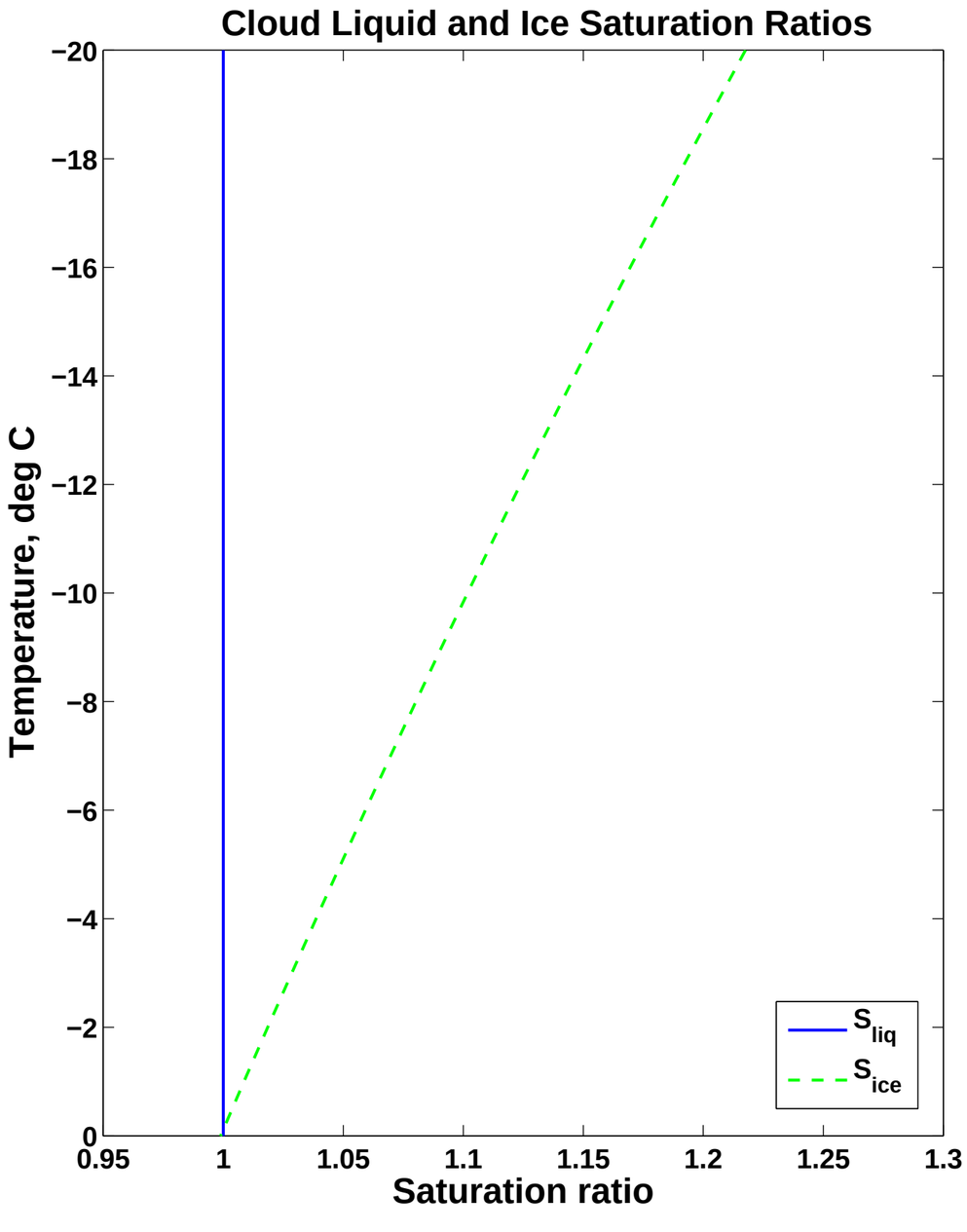
Cloud Liquid and Ice Saturation Ratios
Temperature, deg C
Saturation ratio
−20
−18
−16
−14
−12
−10
−8
−6
−4
−2
0
0.95
1
1.05
1.1
1.15
1.2
1.25
1.3
S liq
S ice

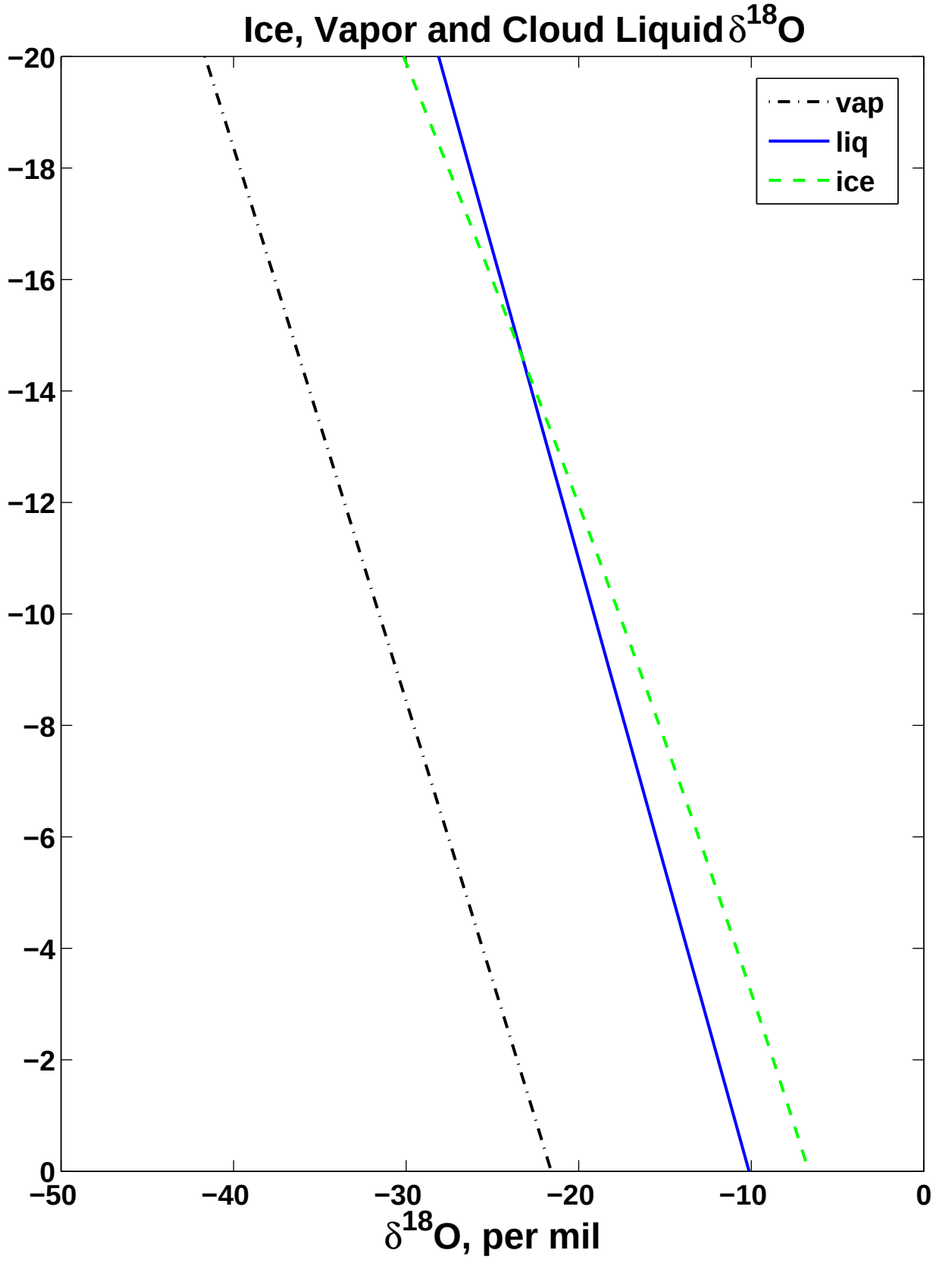
Ice, Vapor and Cloud Liquid δ18O
δ18O, per mil
−20
−18
−16
−14
−12
−10
−8
−6
−4
−2
0
−50
−40
−30
−20
−10
0
vap
liq
ice